Facility for λ_c deuteron production in ALICE

Relatore:
Prof. Andrea Alici

Correlatore:
Dott. Nicolò Jacazio

Presentata da:
Giuseppe Luciano

Contents

Ringraziamenti

Un grazie speciale è dedicato a tutti i compagni di viaggio, sia a chi mi è stato vicino nelle interminabili ore sui treni che a quelli che mi hanno accompagnato durante il percorso accademico. I primi che con mirabile genitilezza si facevano annoiare dai miei racconti ma che erano sempre pronti a ricordarmi che esiste altro oltre a quello che posso vedere coi miei occhi. I secondi invece mi hanno isegnato ad approcciarmi ad una disciplina tanto affascinante quanto ostica fungendo da inesauribile fonte di ispirazione nel mostrarmi i possibili modi di interfacciarsi ai problemi, ognuno con la propria strategia. Sono stati compagni di interminabili e stravagnati conversazioni dal moto caotico ed imprevedibile, perchè spesso non lo si faceva per il risultato ma più per la genuina voglia di ragionare insieme. Sempre di fretta e sempre senza tempo eppure non si iniziava a lavorare seriamente senza prima aver proposto quell'improbabile argomento che ci bloccava per ore. Grazie ai miei grandi amici su cui ho sempre potuto contare anche se il tempo a loro dedicato non gli ha mai reso gustizia. A tutte quelle volte in cui non potevo uscire e a tutte le volte che mi hanno perdonato perchè se ti presenti con una bottiglia cola sarebbe semplicemente folle continuare a tenere il broncio. Ma infine il pensiero principale è diretto ai miei genitori che anche se tornavo tardi avevano comunque la pazienza di aspettarmi per cena, che mi coccolavano nelle torride giornate di studio estivo con dell'acqua al limone ma nel bicchiere bello perchè anche l'occhio vuole la sua parte, che mi riportavano con i piedi per terra perchè a volte la fantasia ti stacca dal suolo, che a volte il vento non gonfia le vele ma la destinazione è lontana e bisogna remare, che a volte in certe serate persino la luna sembra più vicina, e che a volte serve una tesi per capire che non potrò mai ringraziarli abbastanza per tutti i sacrifici che hanno fatto per me.

Chapter 1

Abstract

Recent development of hadron spectroscopy revealed that there may exist various molecular bound states of hadrons (observed as hadron resonances). In particular, lot different study, the observation of the unexpected X, Y, and Z mesons and the follow by theoretical studies indicates that heavy quark molecules are more plausible. This can be understood from the balance between the kinetic term and the potential in the Hamiltonian: a heavier system has a smaller kinetic energy. The above naive expectation motivates us to explore possible bound states composed of is, of course, a natural extension of the hypernucleus, which is a nuclear bound state with played a key role in analysing structures of hypernuclei and extracting information on the and it is difficult to perform direct scattering experiments for the hyperons, it is important to get information on their interactions from the three-body or heavier nucleus with strange baryon(s).

There has been an impressive experimental progress in the spectroscopy of heavy hadrons, mainly in the charm sector. The theoretical analysis of hidden and open heavy flavor hadrons has revealed how interesting is the interaction of heavy hadrons, with presumably or resonances in the scattering of two hadrons with heavy flavor content. The observation of events that could be interpreted in terms of the decay of a charmed nucleus [13, 14], fostered conjectures about the possible existence of charm analogs of strange hypernuclei [15–17]. This resulted in several theoretical estimates about the bind- ing energy and the potential-well depth of charmed hypernuclei based on one-boson exchange prospects have reinvigorated studies of the low-energy YcN interactions

Chapter 2

Concepts of quantum chromodynamics (QCD)

Before talking about heavy-ion collision we should introduce some concepts coming from quantum chromodynamics (QCD) and standard model(SM). The SM describes the universe on the most fundamental level and correctly predicts many of the results of experiment that we have ever done, sometimes with unprecedented levels of accuracy. This theory assumed that the particle can interact together with tree different force: the strong nuclear force, the weak nuclear force, and electromagnetism. The force of gravity is not yet part of the Standard Model but it's straightforward to include it by coupling to a dynamical, curved spacetime [**quevedo2024cambridgelecturesstandardmodel**]. Fortunately the absence of a quantum gravity theory, that is maybe the most fundamental lack of the SM, is not too influent in the experiment that we can actually perform. In fact physicist believe that the gravity influence will became evident only at the plank scale. This region may be characterized by particle energies of around 10^{19} GeV or 10^9 J on a single particle. The same energy of a Jumbo jet. However this theory is very extended and will be focus only on essential aspect for understand the following chapter. The QCD is the most successful theory to explain the strong interaction between quarks mediated by gluons. The quark are elementary particle introduced by Gell-Mann and Zweig for understand the "proliferation of the hadron". In fact when the energy of the collision start to increase different particle that interact with the strong force, hadrons, were discovered. So, for explain the hundred of different hadrons detect, the two scientist proposed that this structures come form different combination of more fundamental particle, the quark. In particular the name quark come from the Finnegan's wake, a book of James Joice. Writer that Gell-Mann love. Instead the quantum chromodynamics takes it's name because it introduces a property called color, the QCD analog of electric charge. Gluons are the force carriers of the theory, just as photons are for the electromagnetic force in quantum electrodynamics. First hint about the real existence of color charge was given with the discovery of

Δ^{++} baryon in 1951. This baryon could be explained only imaging that it is composed of three quark u with the spin aligned observing it's mass end the spin of 3/2 of the baryon. so the configuration of the particle could be written as follows

$$|\Delta^{++}\rangle = |u_\uparrow u_\uparrow u_\uparrow\rangle$$

A highly symmetric configuration. However, since the the particle is a fermion, it must have an overall antisymmetric wave function. In 1965, fourteen years after its discovery, this problem was finally understood by the introduction of the charge of colour. With this new parameter we can add another inner space associated to the particle and is configuration can be written as.

$$|\Delta^{++}\rangle = |u_\uparrow u_\uparrow u_\uparrow\rangle \, \epsilon_{ijk} \, [C_i \otimes C_j \otimes C_k]$$

where ϵ_{ijk} is the Ricci's tensor. Many other strong support of the assumption had been discovered with the passing of time. Quantum Chromodynamics is based on the gauge group SU(3), the Special Unitary group in 3 (complex) dimensions, whose elements are the set of unitary 3×3 matrices with determinant one. Since there are 9 linearly independent unitary complex matrices, the condition on the determinant reduced the set at 8 independent directions in this matrix space, corresponding to eight different generators of the group. The Lagrangian density of QCD is

$$\mathcal{L} = i\bar{\psi}_q^i \gamma^\mu (D_\mu)_{ij} \psi_q^j - m_q \bar{\psi}_q^i \psi_{iq} - \frac{1}{4} F_{\mu\nu}^a F^{a\mu\nu} \tag{2.1}$$

where ψ_q^j denotes a quark field with colour index, γ^μ is a Dirac matrix that expresses the vector nature of the strong interaction, with μ being a Lorentz vector index, m_q, the mass of the quark, allows for the possibility of non-zero quark masses, $F_{\mu\nu}^a$ is the gluon field strength tensor for a gluon and D_μ is the covariant derivative in QCD given by $(D_\mu)_{ij} = \delta_{ij}\partial_\mu - ig_s t_{ij}^a A_\mu^a$, with g_s the strong coupling [**Skands˙2013**]. The last parameter is maybe the most important in defying the properties of the theory, we can imaging it as the probability that a partons, therm used for indicate both gluon and hadrons, of interact at every instant whit other partons. Since this value is considerable during a process the higher order Feynman diagram cannot be neglected and so is particular difficult to perform analytical calculus. So, as it is said in this cases, the theory is not perturbatively tractable. The QCD exhibit three salient poperies: Color confinement, asymptotic freedom and the chiral symmetry breaking. Starting from the first one we can say that unlike one may think watching at Eq 2.1 since the gluon are massless the QCD should be a long range force. Instead the common experience tell us that only at very close distances the effect of the interaction are visible. This is possible because the energy for separate the quark grows until a quark–antiquark pair is spontaneously produced, turning the initial hadron into a pair of hadrons instead of isolating a color charge, a graphical resume is visible in Fig 2.1.
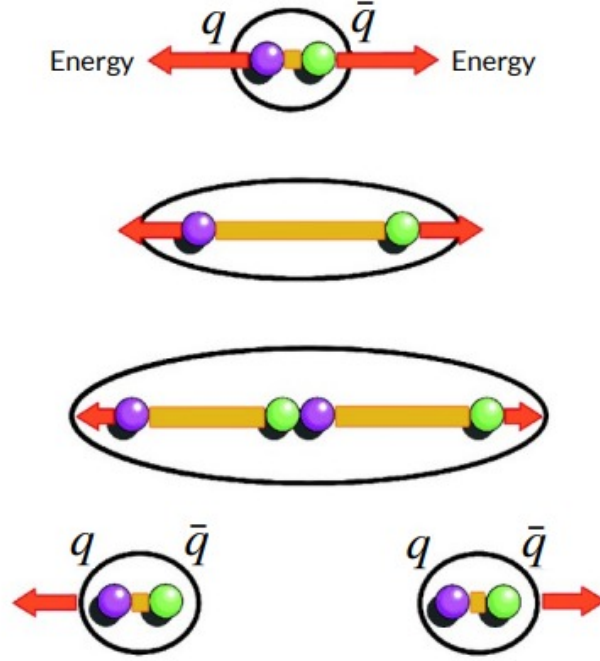
Figure 2.1: The figure resume the process of pair production of quark. **??**

This is a very efficient way for dissipate the energy and the final result is the
production of jets of hadron clearly visible in the experimental data. The
physicist believe that a direct consequence of the theory is the "confinement
of hadrons" that exclude the possibility of find free quark. A formal proof
had not been yet obtained and this problem has been added to the list of the
Millennium Prize Problems.

The asymptotic freedom is a reduction in the strength of interactions be-
tween quarks and gluons as the energy scale of those interactions increases.
In fact if in a collision the transferred momenta is low we can study it with
a little De Broglie wave length and so we cannot penetrate the cloud of vir-
tual process. Instead if the transferred momenta increase we can penetrate
deeper in the virtual process cloud and so see in more detail the "naked par-
ticle" and so see analyze different behaviors of this latter. The asymptotic
freedom of QCD was discovered in 1973 by David Gross and Frank Wilczek,
[**DAVIDPOLITZER1974129**]. and independently by David Politzer in the
same year. For this work, all three shared the 2004 Nobel Prize in Physics.
The asymptotic freedom is related to the fact that the quark-antiquark loop
has a shielding effect of the charge and the gluon loop has an anti screening
effect. In particular hold that for the coupling constant that.

$$g_s(Q^2) = \frac{g_s(\mu^2)}{1 + g_s(\mu^2)\frac{11n_c - 2n_f}{12\pi}\ln\left(\frac{Q^2}{\mu^2}\right)} = \frac{g_s(\mu^2)}{1 + g_s(\mu^2)\frac{21}{12\pi}\ln\left(\frac{Q^2}{\mu^2}\right)} \tag{2.2}$$

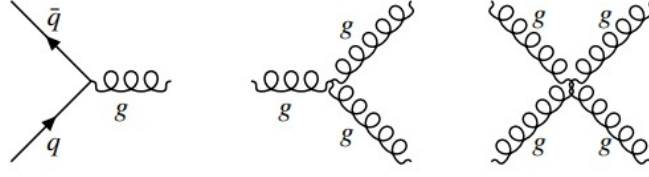where μ is a generic transferred quadri-momenta as Q, n_f is the number of

Figure 2.2: The figure show the basilar Feynman diagram of QCD.

known flavor(assumed 6 in the SM), n_c the number of color (assumed 3). Is possible to observe that $11n_c > 2n_f$ and for these reason the anti-shielding effect of the gluon loop is prevalent. From the Eq 2.2 we can desume that the coupling decrease when the transferred momenta increase. the Eq 2.2 is usually expressed showing the scale factor.

$$g_s(Q^2) = \frac{1}{\frac{1}{g_s(\mu^2)} + \frac{21}{12\pi} \ln\left(\frac{Q^2}{\mu^2}\right)} \tag{2.3}$$

defining

$$\frac{1}{g_s(\mu^2)} = \frac{21}{12\pi} \ln\left(\frac{\mu^2}{\Lambda_{CQD}^2}\right) \tag{2.4}$$

$$g_s(Q^2) = \frac{1}{\frac{21}{12\pi} \ln\left(\frac{\mu^2}{\Lambda_{CQD}^2}\right) + \frac{21}{12\pi} \ln\left(\frac{Q^2}{\mu^2}\right)} = \frac{1}{\frac{21}{12\pi} \ln\left(\frac{Q^2}{\Lambda_{CQD}^2}\right)} \tag{2.5}$$

In this way is more evident the point that made the logarithm diverge. Experimentally it is found $\Lambda \sim 300$ Mev.[**Semprini**] With the deployment of computers it has become possible to perform lattice QCD simulations. These simulations allow for the non-perturbative study of the strong interaction by discretizing spacetime into a lattice, which makes it feasible to numerically calculate the behavior of quarks and gluons. Prior to the advent of these advanced computational resources, such detailed simulations were impractical due to the immense complexity involved in solving QCD equations at low energies.

In conclusion we can talk about the Chiral symmetry breaking. Massless fermions in Dirac theory are described by left or right-handed spinors. The difference is related to the fact that a particle can have spin either aligned (right-handed chirality), or counter-aligned (left-handed chirality), with his momenta. In this case chirality is a conserved quantum number of the fermion and the description of the can be spinous can be reduced in these space. A Dirac mass term explicitly breaks the symmetry but in QCD, the lowest mass quarks are nearly massless and exist an approximate chiral symmetry. The vacuum in QCD is non-trivial. It does not simply consist of empty space but it has a rich structure in which quark-antiquark pairs are continually being created and annihilated. This is sometimes referred to as the QCD vacuum. This

vacuum is described as a superposition of many states, and the interactions between quarks and gluons cause the system to prefer a certain configuration, which spontaneously breaks the chiral symmetry. The spontaneous symmetry breaking generate masses for hadrons far above the masses of the quarks, and making pseudoscalar mesons exceptionally light. Yoichiro Nambu was awarded the 2008 Nobel Prize in Physics for elucidating the phenomenon in 1960. Lattice simulations have confirmed all his generic predictions.

For our discussion the Polyakov loop operator gets a particular importance.

$$L = \frac{1}{3}Tr\left(Pe^{ig\int_0^\beta d\tau A_4(\vec{x},\tau)}\right) \tag{2.6}$$

Where P is the path-ordering operator and $A-4$ is the Euclidean temporal component of the gauge field and $\beta = \frac{1}{T}$, T temperature. A vanishing thermal expectation value $\langle L \rangle$ of the Polyakov loop operator thus indicates infinite energy for a free quark, i.e. quark confinement. Studying the equation became evident that as the temperature increases $\langle L \rangle$ increases rapidly to a nonzero value at high temperatures. This indicates that quark confinement is broken at the corresponding critical temperature T_{cr}. In the absence of quark masses the equation 2.1 is chirally symmetric. Since the up and down quark masses are very small, neglecting them is a good approximation. The nonvanishing chiral condensate at T = 0 breaks this chiral symmetry and generates a dynamic mass, the so called "constituent" masses. In vacuum this mass are thus about 300 MeV for the up and down quarks, about 450 MeV for the strange quark, 1.5 Gev for the charm, 4.5 Gev for bottom and 180 Gev for top. The dynamically generated mass disappeared at T_{cr} , making the quarks light again and restoring the approximate chiral symmetry of QCD. The dissolution of massive hadrons into almost massless quarks and gluons at T_{cr} leads to a very rapid rise of the energy density near the deconfinement transition, as shown in Fig 2.3. For a massless gas of quarks and gluons the energy density is proportional to T^4. We see that for T ¡ $4T_{cr}$ the data remain about 20% below this Stefan-Boltzmann limit. Instead near T_{cr} the ratio ϵ/T^4 drops rapidly by more than a factor 10. This is due to hadronization. The much heavier hadrons are exponentially suppressed below T_{cr}, leading to a much smaller number of equivalent massless degrees of freedom. The dependence of T^4 is particularly important because for exceed the critical temperature by only 30% in order to reach the upper edge of the transition region, an energy density $\epsilon \approx 3.5$ GeV/fm^3 is required and to reach $2T_cr$ the energy density needed arrived at 23 GeV/fm^3 [**heinz2004conceptsheavyionphysics**].

2.0.1 The QCD phase diagram

In QCD the only viable option to free the hadron constituents is to increase significantly the energy scale of the system by compression or by heating. At this high energy regime hadronic matter melts releasing its elementary
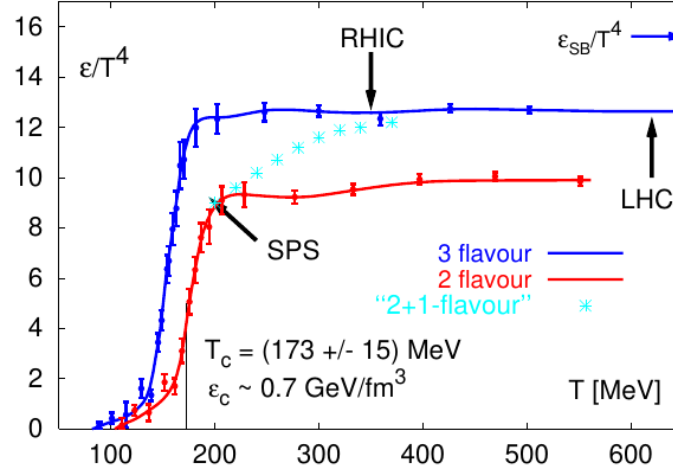
Figure 2.3: The symbol ϵ stands fo energy density, the curves labelled "2 flavour" and "3 flavor" were calculated for two and three light quark flavors, "2+1 flavour" indicates a calculation for two light and one heavier strange quark flavor.

degrees of freedom (quark and gluons) in a way which is analogous to a phase transition. A simple description of the phases of nuclear matter is given in Fig 2.4. In order to gain insight into the dynamics of the QCD phase, many studies were performed by using lattice QCD calculations. The Quark Gluon
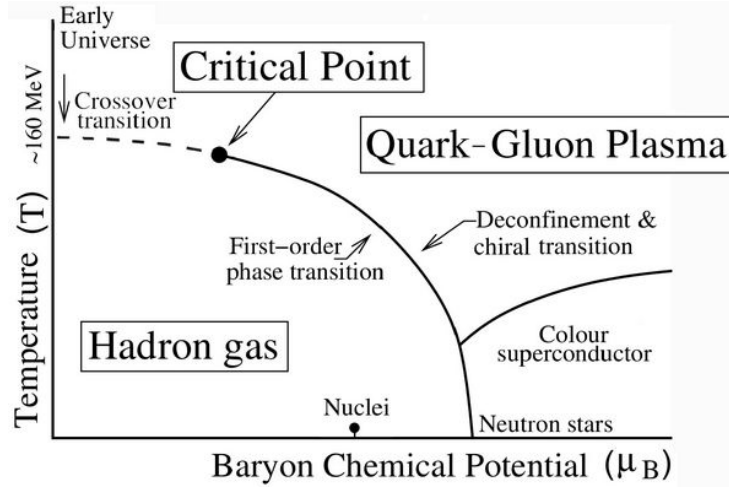
Figure 2.4: A sketched view of the phase diagram of strongly interacting matter, in the plane of temperature and the baryon chemical potential that represents the amount of net baryon charge available in the system

Plasma (QGP) is hottest and most dense liquid known to humankind and, according to the most widely accepted cosmological model, the ΛCDM, were the condition of our universe only few microseconds after the Big Bang. The chemical potential is a thermodynamic coordinate like the temperature, which can be best understood as the energy required by the system to change its chemical composition . It is tightly connected with the density of quarks: when the former is zero, the latter is zero as well. [**QCDPhase-Diagram**].

Particularly problematic is the study of the diagram when μ_B approaches 0, like in the condition of the primordial universe. Lattice QCD tells us that even for realistically small up and down quark masses the transition at $\mu_B = 0$ is most likely not a sharp phase transition but a rapid crossover as shown in Fig 2.4. At low temperatures and asymptotically large baryon densities quarks are also deconfined, although not in a quark-gluon plasma state but rather in a color superconductor, in these state matter carries color charge without loss, analogous to the conventional superconductors that can carry electric charge without loss. The superconducting state is separated from the QGP by a first order transition at a critical temperature estimated to be of order 30-50 MeV. Unfortunately, one cannot use heavy-ion collisions to compress nuclear matter without producing a lot of entropy and therefore also heating it; hence it seems impossible to probe with them the color superconducting phase [**heinz2004conceptsheavyionphysics**].

2.0.2 The different stage of a heavy-ion collision

The main stages of relativistic heavy-ion collisions are: Pre-equilibrium, thermalization, Chemical freeze-out, and decoupling. This section came mainly from [**heinz2004conceptsheavyionphysics**] and [**amsdottorato9036**].

1. Pre-equilibrium (t ¡ 1 fm/c): the two nuclei just collided. The partons of every participating nucleon interact producing a large amount of quarks and gluons. The system is now formed by a dense inhomogeneous droplet of strongly interacting QGP matter. In the very early collision stages the momentum transferred is huge and the particle production can be calculated in perturbative QCD. However the strong force is the first that manifest it's effect. According to the Heisemberg uncertainty relation the production happens on a time scale $t \sim \frac{1}{\sqrt[2]{Q^2}}$, where Q is the momentum transfers. The key difference between elementary particle and nucleus-nucleus collisions is that the quanta created in the primary collisions between the incoming nucleons can't right away escape into the surrounding vacuum, but rescatter of each other. In a central collision between two Pb or Au nuclei the nuclear reaction zone has a transverse diameter of about 12 fm, so a hard particle created near the edge and moving towards the center needs 12 fm/c before it emerges on the other side. During this time the matter thermalizes, expands, cools down and almost reaches decoupling. It does so by scattering off the evolving medium and losing energy which can be measured. The energy loss is proportional to the density of the medium times the scattering cross section between the probe and the medium constituents, integrated along the probe's trajectory. Other probes of the early collision stage are direct photons, either real or virtual, and other process connected to QED such the creation of a couple lepton-antilepton generally known as

"dileptons". In contrast to all hadronic probes, they thus escape from
the collision zone without reinteraction and carry pristine information
about the momentum distributions of the particle that generated them.
Unfortunately, the directly emitted photons and dileptons must be must
be searched in a huge background of indirect photons and particle gen-
erated in other process, This renders the measurement of these clean
electromagnetic signals difficult.

2. Thermalization ($t \sim 1 \div 10$ fm/c): the medium reaches thermal equilib-
rium thanks to the many interactions and the formations of new parton.
The produced partons rescatter both elastically and inelastically. Both
types of collisions lead to equipartitioning of the deposited energy, but
only the inelastic collisions change the "chemical" composition of the
medium by changing the flavor of partons. The system, now in equilib-
rium, builds an internal pressure that finds no opposition by the void
that surrounds it. This leads to a rapid expansion of the system together
with a decrease in the temperature. As the temperature lowers, the sys-
tem energy density is not able to keep partons separated and hadrons
start to form when the energy density approach $\epsilon \approx 1 \, \text{GeV}/fm^3$. During
this phase transition the entropy density drops because of the recombi-
nation. However the total entropy cannot decrease this implies that the
fireball volume must increase by a large factor while the temperature
remains approximately constant. Since the recombination take times
the systems spend significant time near T_cr.

3. Chemical freeze-out: when the temperature decreases enough inelas-
tic interactions among hadrons have completely stopped and only the
(pseudo-)elastic one occur. This happen because at this point the matter
becomes so dilute that the average distance between hadrons exceeds the
range of the strong interactions. The hadrons abundance "freeze out"
but the creation of some resonance is however possible but such pro-
cesses don't change the finally observed chemical composition. Since
most of the hadrons in a relativistic fireball are pions, very light particle
$m_\pi \sim 140$ MeV, resonances with them are very efficient in keeping the
system in thermal equilibrium.

4. Kinetic freeze-out: at this stage the hadrons,including the then present
unstable resonances, start to decouple from the medium as the tem-
perature lowers and the mean free path becomes larger than the mean
distance between hadrons. This results in a complete stop of all inter-
actions. Now the repartition of the kinetic energy among all hadrons
has stopped and the transverse momentum spectrum is approximately
exponential. The unstable resonances decay in particle with smaller
transverse momenta. Since most resonances decay by emitting a pion,
this effect is particularly important for the pion spectrum which at low

$p_\perp$ are completely dominated by decay products.

A graphical resume of the process is visible in Fig 2.6 and 2.5

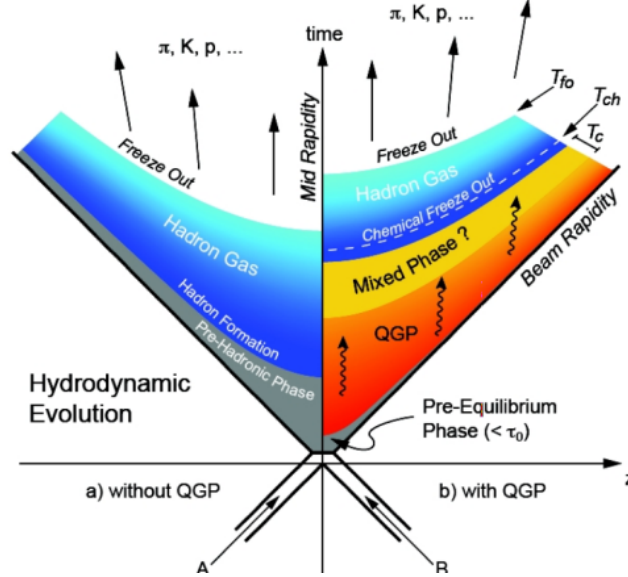Figure 2.5: Evolution of a central heavy ion collision in a Minkowski-like plane. The two scenarios with and without QGP are pointed out. The critical temperature is indicated by T_c, while the freeze-out and chemical freeze-out temperatures, are pointed out with T_{fo}, and T_{ch}, respectively [**EvolutionofcollisionsandQGP**].
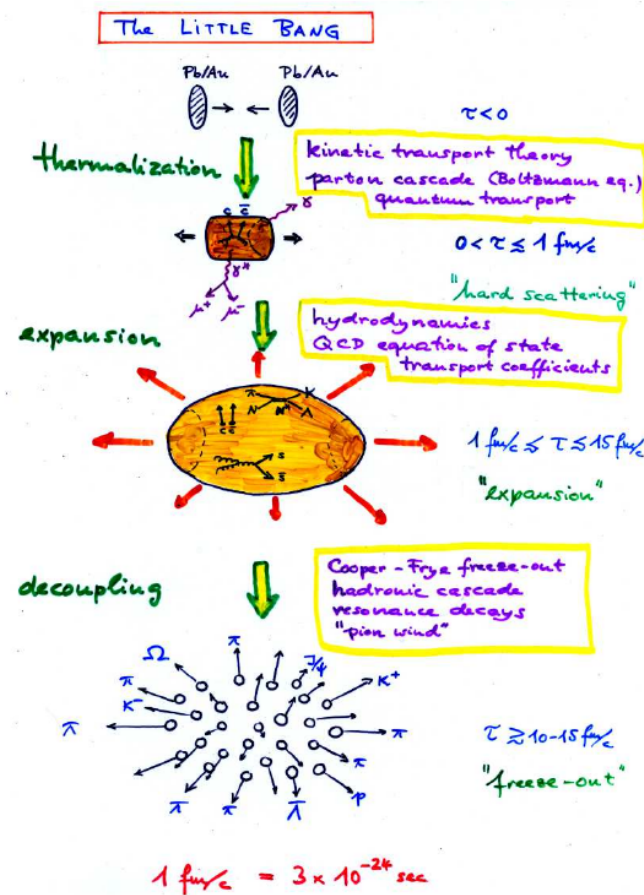
Figure 2.6: A sketched view of the phase of the system after the collision

Chapter 3

Thermal model

3.0.1   hydrodynamical description

This section resume the information of [**heinz2004conceptsheavyionphysics**], [**phdthesis**], [**Cooper-Frye**].

The fireball can be approximately described as an ideal fluid if the microscopic scattering time scale is much shorter than any macroscopic time scale associated with the fireball evolution. Hydrodynamics becomes applicable when the mean free path of the particles is much smaller than the system size, and allows for a description of the system in terms of macroscopic quantities.The hydrodynamic equations require knowledge of the equation of state that in this case must connect the pressure, the energy density and baryon density. Hydrodynamics is the ideal language for relating observed collective flow phenomena because it allows ad description of the hadronization phase transition without any need for a microscopic description.

For define the collective flow we can consider any space-time point in the fireball and considered an infinitesimal volume associate with the point. So the flow velocity can be expressed by $\vec{v}(x) = \frac{\vec{P}}{P^0}$, where $\vec{P}$ is the mean 3-momentum of the particle in the volume and P^0 is the mean energy in quadrivectorial formalism. With $\vec{v}(x)$ we can associate a normalized velocity $u^\mu = \gamma(\vec{v}(x) = \frac{1}{\sqrt[2]{1-v(x)^2}})$ In the same manner it's we define T(x) the average local temperature and the μ_i, the chemical potential of the i-th particle species. It's possible to separate the flow velocity into its components along the beam direction ("longitudinal flow" $\vec{v}_l(x)$) and in the plane perpendicular to the beam ("transverse flow" $\vec{v}_\perp(x)$). From now on we use the unit c=1, $\hbar$=1. In this case the phase-space distribution of particles of type i is given by the Lorentz covariant local equilibrium distribution

$$f_{i,eq}(x,p) = \frac{g_i}{e^{(p \cdot u - \mu_i)/T} \pm 1} = g_i \sum_{n=1}^{\infty} (\pm)^n e^{n(p \cdot u - \mu_i)/T} \tag{3.1}$$

Here gi is a spin-isospin-color-flavor-etc. degeneracy factor which counts all particles with the same properties. The factor $p \cdot u$ is the energy of the

particle in the local rest frame. The ± 1 in the denominator accounts for the proper quantum statistics of particle (-1 for fermions and +1 for boson). The Boltzmann approximation corresponds to keeping only the first term in the sum over n in the last expression. In our applications this is an excellent analytical approximation for all hadrons except for the pion because of their mass.

At relativistic energies it is convenient to parametrize the longitudinal flow velocities and momenta in terms of rapidities, $\eta = \frac{1}{2}ln\frac{1+v}{1-v}$ in this way $v = tanh(\eta)$. It's also possible to define $\eta_l = \frac{1}{2}ln\frac{1+v_l}{1-v_l}$ and $y = \frac{1}{2}ln\frac{1+\frac{p_l}{E}}{1-\frac{p_l}{E}} = \frac{1}{2}ln\frac{E+p_l}{E-p_l}$. Bjorken argued that at asymptotically high energies the physics of secondary particle production should be independent of the longitudinal reference frame. Furthermore, the boost-invariance of these initial conditions is preserved in longitudinal proper time if the system expands collectively along the longitudinal direction, in this approximation hold $\eta = \eta_l$. For more detail see [**PhysRevD.27.140**]. The Bjorken scaling approximation is expected to be good at high energies and not too close to the beam and target rapidities, i.e. in safe distance from the longitudinal kinematic limits. Whit Bjorken intuition.

$$p \cdot u(x) = \gamma_\perp(\vec{r}_\perp, \tau) \left(m_\perp cosh(y - \eta) - \vec{p}_\perp \cdot \vec{v}_\perp(\vec{r}_\perp, \tau) \right) \qquad (3.2)$$

Where $\vec{r}_\perp = (x, y)$, $m_\perp = \sqrt{m^2 + p_\perp^2}$ is the transverse mass, $\tau = \sqrt{t^2 - z^2}$ is the longitudinal proper time and z the longitudinal position.

The Cooper-Frye formula

Suppose we want to count the total number of particles of species i after produced in the collision. Since this number does not depend on the reference frame of the observer, we must be able to express it in a Lorentz-invariant way. We define a three-dimensional hypersurface $\Sigma(x)$ in 4-dimensional space-time along which we perform the counting. Different choices for the 3-dimensional hypersurface Σ are possible as long as it completely closes off the future light cone emerging from the collision point. We count particles crossing the surface by subdividing it into infinitesimal elements $d^3\sigma$, defining an outward-pointing 4-vector $d^3\sigma_\mu(x)$ perpendicular to $\Sigma(x)$ at point x with the magnitude $d^3\sigma$. Introducing the 4-vector j_i^μ describing the current of particles i through point x, and summing over all the infinitesimal hypersurface elements we get

$$N_i = \int_\Sigma d^3\sigma_\mu(x)\, j_i^\mu(x) = \int_\Sigma d^3\sigma_\mu(x) \left(\frac{1}{(2\pi)^3} \int \frac{d^3p}{E}\, p^\mu f_i(x, p) \right) \qquad (3.3)$$

Where $j_i^\mu(x)$ is given in terms of the Lorentz-invariant phase-space distribution (giving the probability of finding a particle with momentum p at point

x) by multiplying it with the velocity $\frac{p^\mu}{E}$ and integrating over all momenta with measure $\frac{d^3p}{(2\hbar\pi)^3} = \frac{d^3p}{(2\pi)^3}$. We finally obtain the Cooper-Frye formula

$$\boxed{E\frac{dN_i}{d^3p} = \frac{dN_i}{dy\,p_\perp\,dp_\perp\,d\phi_p} = \frac{dN_i}{dy\,m_\perp\,dm_\perp\,d\phi_p} = \frac{1}{(2\pi)^3}\int_\Sigma p\cdot d^3\sigma_\mu(x)f_i(x,p)}$$

(3.4)

with ϕ_p is the azimuthal angle. To compute the measured momentum spectrum we can therefore replace the surface Σ corresponding to the detector by shrinking it to the smallest and earliest surface that still encloses all scattering processes. We call this the "surface of last scattering" or "freeze-out surface" Σ_f. The the number of particles obtained from the Cooper-Frye formula is not always positive-definite. Physically negative contributions of the Cooper-Frye formula are particles that stream backwards into the hydrodynamical region. It's possible to compare the negative contribution with the total number particles crossing the transition hypersurface. It is found that the number of underlying inward crossings is much smaller than the one the Cooper-Frye formula gives under the assumption of equilibrium distribution functions.

to compute the measured momentum spectrum requires knowledge of the phase-space distribution on the surface of last scattering If the system expands very fast, its density decreases rapidly and the mean free path of the particles growth quickly. The transition from strong coupling to free-steaming thus happens in a short time interval. During this short time it is unlikely that the phase-space distribution undergoes qualitative changes, and we may approximate $f_i(x,p)$ on the last scattering surface by its thermal equilibrium form that it still had just a little earlier. In this section we report only the final result but the proof could be find in the appendix.

$$\frac{dN_i}{dy\,m_\perp\,dm_\perp} = \frac{g_i}{\pi^2}\int_0^\infty r_\perp\,dr_\perp\,n_i(r_\perp)\left[m_\perp K_1\left(\frac{m_\perp\cosh(\rho(r_\perp))}{T(r_\perp)}\right)I_0\left(\frac{p_\perp\sinh(\rho(r_\perp))}{T(r_\perp)}\right)\right.$$
$$\left.-p_\perp\frac{\partial\tau}{\partial r_\perp}K_0\left(\frac{m_\perp\cosh(\rho(r_\perp))}{T(r_\perp)}\right)I_1\left(\frac{p_\perp\sinh(\rho(r_\perp))}{T(r_\perp)}\right)\right]$$

(3.5)

Where appear the modified Bessel functions and $v_\perp = tanh\rho$. This formula is useful because it allows to easily perform systematic studies of the influence of the radial profiles of temperature, density and transverse flow on the transverse momentum spectrum, in order to better understand which features of a real dynamical calculation of these profiles control the shape of the observed spectra.

Eq 3 can be simplified by assuming instantaneous freeze-out at $r_T = R$, The freeze-out volume. In this case there is no dependence of the proper time at the freeze-out surface τ therefore $\frac{\partial\tau}{\partial r_\perp}$ so we can rewrite the previus equation in the following manner.

$$\frac{dN_i}{dy\, m_\perp\, dm_\perp} = \frac{g_i}{\pi^2} \int_0^\infty r_\perp\, dr_\perp\, n_i(r_\perp) \left[m_\perp K_1 \left(\frac{m_\perp \cosh(\rho(r_\perp))}{T(r_\perp)} \right) I_0 \left(\frac{p_\perp \sinh(\rho(r_\perp))}{T(r_\perp)} \right) \right]$$
(3.6)

Commonly named Boltzmann-Gibs blast wave. This formulation is particularly used for extract properties of the common source such as the temperature T_f or to fit the single particle spectra. The agreement of Eq 3.6 with the spectra is quite remarkable especially in central events where the thermal description is expected to work better. Conversely, for peripheral collisions the two fits give quite different results.

Transverse momentum spectra and freeze-out temperature

For all hadrons is observed that $m_\perp/T > 1$ so the modified Bessel function can be approximate in the following manner $K_\nu \sim e^{-\frac{m_\perp \cosh \rho}{T}}$. Since temperature on the freeze-out hypersurface is approximately constant and that the freeze-out volume is controlled by the mean free path which is inversely proportional to the density, which itself is a steep function of temperature. At $r_\perp = 0$ the radial flow velocity must vanish by symmetry but to larger $r_\perp$ typically rises linearly. , it eventually reaches a maximum value and drops again to zero since the dilute tail of the initial density distribution freezes out early. Some simulated profile of grow are shown in the Fig 3.1 [**teaney2001hydrodynamicdescriptionheavyion**].
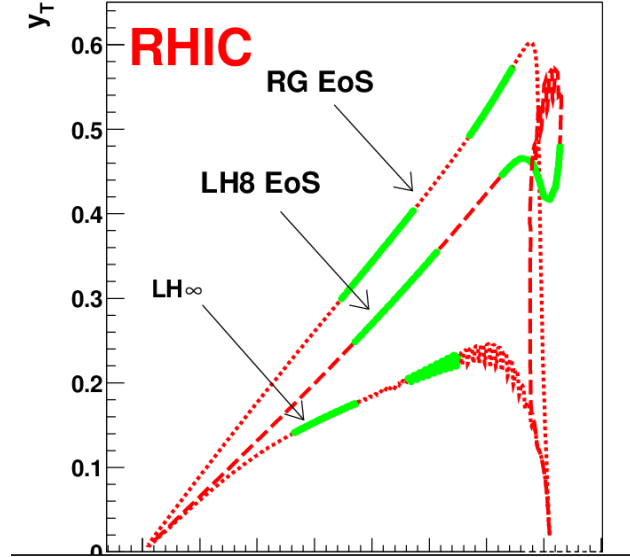

Figure 3.1: Radial flow rapidity profile $\rho(r_\perp) = y_T$ for central Au+Au collisions at RHIC, from hydrodynamic calculations employing three different equations of state [**EvolutionofcollisionsandQGP**].

Different process can manifest, for example at SPS energies the freeze-out surface moves from the edge inward since the fireball matter cools and

freezes out faster than the developing radial flow can push it out. At LHC energies the much stronger radial flow generated by the much higher internal pressure makes the fireball grow considerably before suddenly freezing out after about 13 fm/c. For understand how the radial flow influence the spectra first consider the absence of flow ($\rho = 0$), in this condition $I_q(0) = 0$ so the equation 3.5 reduced to

$$\frac{dN_i}{dym_\perp dm_\perp} \sim m_\perp K_1 \left(\frac{m_\perp}{T}\right) \sim m_\perp^{1/2} e^{-\frac{m_\perp}{T}} \tag{3.7}$$

In these condition as the temperature is the same for all hadron the spectra depend only on the transverse mass, a fact known as "$m_\perp$" scaling. As visible in the equation the temperature can be extracted easily. Instead if the radial flow is not vanishing approximating $p_\perp \approx m_\perp$ one get.

$$\frac{dN_i}{dym_\perp dm_\perp} \sim e^{-\frac{m_\perp(\cosh\rho-\sinh\rho)}{T}} = e^{-\frac{m_\perp}{T_{slope}}} \tag{3.8}$$

With $T_{slope} = T\sqrt{\frac{1+v_\perp}{1-v_\perp}}$ It is most extreme for a thin shell expanding with fixed velocity ("blast wave"), shown in Fig 3.2, in which case for sufficiently large hadron mass and flow velocity the spectrum develops a blast wave peak at nonzero transverse momentum. In conclusion is possible to summarize these two important limits

$$\text{Non relativistic:} \quad p_\perp \ll m_i \qquad T_{i,\text{slope}} \approx T_f + \frac{1}{2}m_i\langle v_\perp\rangle^2 \tag{3.9}$$

$$\text{Relativistic:} \quad p_\perp \gg m_i \qquad T_{\text{slope}} = T\sqrt{\frac{1+v_\perp}{1-v_\perp}} \tag{3.10}$$

This effect are visible in Fig. 3.2 for two flow velocities. In particular is possible to observe that for small $m_\perp$ the $m_\perp$-scaling is expected to be broken as a consequence of the presence of flow. These formulations have of course their practical limitations in fact pions, the lightest hadrons, are quickly falling into the relativistic case and few measure are performed at low momenta, especially in collider experiments. In addition, non-relativistic pions are affected by both Bose-Einstein statistics and contribution from resonance decays. Furthermore the $m_\perp$-scaling is expected to be more evident for the pp collision while for the heavy-ion case the presence of the radial flow breaks the $m_\perp$-scaling. As expected, radial flow causes a mass-dependent flattening of the spectra in the low $p_\perp$ region, while all spectra start to assume the same slope ad higher momenta. The modification of the spectral shape affects also the mean of the distribution in a mass-dependent way, resulting in an increase of the $p_\perp$ with the particle mass. This increasing is expected to be more evident when flow is stronger i.e. in more energetic collision.
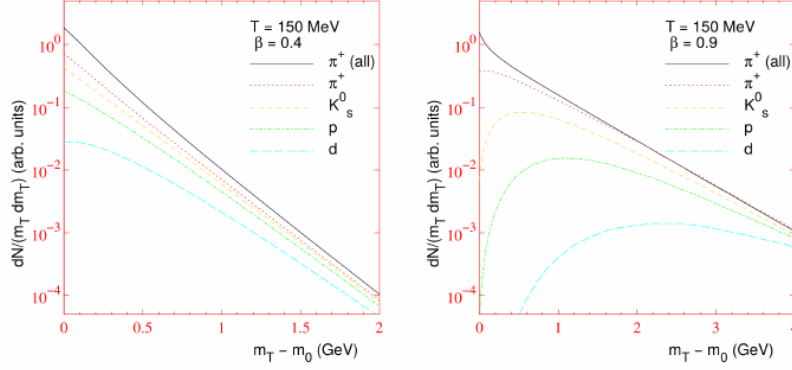
Figure 3.2: Flow spectra for various hadrons as a function of $m_\perp - m_0$ where m_0 is their rest mass. The calculation assumes an infinitesimally thin shell of temperature T = 150 MeV expanding with $v_\perp = 0.9$. The curve labelled "π^+ (all)" includes pions from resonance decays in addition to the thermally emitted pions.
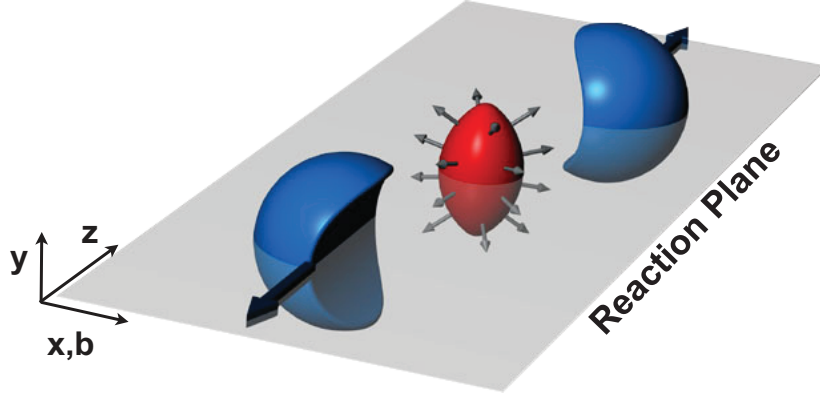

Figure 3.3: Almond shaped interaction volume after a non-central collision of two nuclei. The spatial anisotropy with respect to the x-z plane (reaction plane) translates into a momentum anisotropy of the produced particles (anisotropic flow).

3.0.2   Elliptic flow

this section come from [**Snellings˙2011**], [**heinz2004conceptsheavyionphysics**] [**Kolb˙2000**]. For central collisions between equal spherical nuclei, radial flow is the only possible type of transverse flow allowed by symmetry. In non-central collisions between this azimuthal symmetry is broken and anisotropic transverse flow patterns can develop. The overlap region of the two colliding nuclei is then spatially deformed in the transverse plane. Experimentally, the most direct evidence of flow comes from the observation of anisotropic flow which is the anisotropy in particle momentum distributions correlated with the reaction plane. The evolution of the almond shaped interaction volume is shown in Fig 3.4 [**kolb2003hydrodynamicdescriptionultrarelativisticheavyion**]. The contours indicate the energy density profile and the sequence show the time evolution from an almond shaped transverse overlap region into an almost symmetric system. This expansion happen at the speed of speed velocity $v_s = \sqrt{\frac{\partial p}{\partial \epsilon}}$. In this situation the equation 3.4 can be written using a Fourier
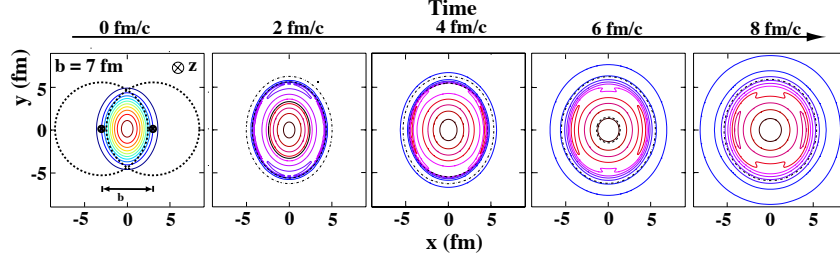
Figure 3.4: The created initial transverse energy density profile and its time dependence in coordinate space for a non-central heavy-ion collision. The z-axis is along the colliding beams, the x-axis is defined by the impact parameter.

expansion and introducing b, the impact parameter, in the form

$$
E\frac{dN_i}{d^3p}(b) = \frac{dN_i}{dy p_\perp dp_\perp d\phi_p}(b) = \frac{1}{2\pi}\frac{dN_i}{dy p_\perp dp_\perp}(b)\left(1 + 2\sum_{n=1}^{\infty} v_2^i(p_\perp, b)\cos(n\phi_p)\right)
$$
(3.11)

In this Fourier decomposition, the coefficients v^1 and v^2 are known as directed and elliptic flow, respectively. The overlap region of the two colliding nuclei is then spatially deformed in the transverse, as visible in Fig 3.3, plane so the momentum space distribution changes in the opposite direction from being approximately azimuthally symmetric to having a preferred direction in the reaction plane. The asymmetry in momentum space can be quantified by the spatial ellipticity:

$$
\epsilon_x(b) = \frac{\langle y^2 - x^2\rangle}{\langle y^2 - x^2\rangle}
$$
(3.12)

As a function of time ϵ_x decreases, spontaneously due to free-streaming radial expansion (if no rescattering happens) or somewhat more quickly due to the development of elliptic flow (if rescattering occurs) which makes the system expand faster into the reaction plane than perpendicular to it. The first mechanism is a consequence of the Heisenberg uncertainty principle because if the definition in the position is higher the uncertainty on the linear momentum in the same direction is higher and the particle can move faster. Instead the elliptic flow is a consequence of the fact that there is high pressure in the interior of the reaction zone which falls off to zero outside. the pressure gradient is so steeper in the short direction, leading to stronger hydrodynamic acceleration. Hydrodynamics predicts that heavier particles gain more momentum than lighter ones, leading to the previously discussed flattening of their spectra at low transverse kinetic energies. It's possible to show that the spatial eccentricity decrease as a function of time in the following manner, the proof is in the appendix.

$$
\frac{\epsilon_x(\tau_0 + \Delta\tau)}{\epsilon_x(\tau_0)} = \left[1 + \frac{(c\Delta\tau)^2}{\langle \vec{r}^2\rangle_{\tau_0}}\right]^{-1}
$$
(3.13)

where τ_0 is the time when the particles were created and $\langle \vec{r}^2\rangle_{\tau_0}$ is the azimuthally averaged initial transverse radius squared of the reaction zone. So

if thermalization is delayed by a time $\Delta\tau$, any elliptic flow would have to build on a reduced spatial deformation and would come out smaller. It is also known from microscopic kinetic studies that for a given initial spatial eccentricity the magnitude of the generated elliptic flow is a monotonic function of the mean free path that can be rewritten by the product of density and scattering cross section in the fireball.

More recently, it was realized that small deviations from ideal hydrodynamics, in particular viscous corrections, already modify significantly the buildup of the elliptic flow. The shear viscosity determines how good a fluid is, however, for relativistic fluids the more useful quantity is the shear viscosity over entropy ratio η_v/s. For perfect fluids the ratio can be approximated by:

$$\frac{\eta_v}{s} \approx \frac{\hbar}{4\pi k_B} \tag{3.14}$$

It is argued that the transition from hadrons to quarks and gluons occurs in the vicinity of the minimum in η_v/s, just as is the case for the phase transitions in helium, nitrogen, and water. The fact that the QGP behaves like an ideal fluid implies strong non-perturbative interactions in the quark-gluon plasma phase.

3.0.3 Statistical Hadronisation Model (SHM)

This section had been inspired by the folowing article [**becattini2009introductionstatisticalhad** [**charm˙hierarchy˙in˙the˙statistical˙hadronization˙model**] [**heinz2004conceptsheavyionp** [**amsdottorato9036**].

The idea of applying statistical concepts to the problem of multi-particle production in high energy collisions dates back to a work of Fermi in 1950, who assumed that particles originated from an excited region evenly occupying all available phase space states. The microscopic description of the process in which thousand of quarks and gluons combine to form thousands of final state hadrons is an impractical problem. Note that such a statistical approach has, of course, its limitations. In fact investigating correlations between pairs, triplets, quadruplets etc. of particles, because they all belong to a single collision and are not produced entirely independently. For example the momenta of thousand of particle emerging from the fireball must conserve the original momentum of the initially colliding nuclei probably generating non-statistical momentum correlations among considerably smaller subclusters of particles. So for describe this complex dynamical process, the Statistical Hadronisation Model (SHM) postulates that hadrons are formed from the decay of each cluster in a purely statistical way so. *Every multihadronic state localized within the cluster and compatible with conservation laws is equally likely.*

The volume of the system created in heavy-ion collisions is considerably larger than the partonic scale, this justifies the usage of a grand-canonical ensemble. Under these conditions the elementary volume under study can

exchange both particles and energy with its surroundings meaning that the quantum numbers are conserved. In particular the volume of clusters is in a constant ratio with their mass when hadronization takes place. In addition one has to consider the quantum behaviour of both fermionic and bosonic degrees of freedom that form the system. Quantum interference effects in the production of identical particles, the so-called Bose-Einstein correlations or Hanbury Brown-Twiss second-order interference would simply be impossible without a finite volume. The Bose-Einstein correlations (BEC) refer to a quantum mechanical phenomenon that arises due to the wave-like nature of bosonic particles and their tendency to occupy the same quantum state. Instead the Hanbury Brown and Twiss (HBT) effect is any of a variety of correlation and anti-correlation effects in the intensities received by two detectors from a beam of particles. HBT effects can generally be attributed to the wave–particle duality of the beam, and the results of a given experiment depend on whether the beam is composed of fermions or bosons. From statistical mechanics is known that hold

$$\langle N \rangle = \frac{1}{\beta} \left(\frac{\partial lnZ}{\partial \mu_B} \right) \tag{3.15}$$

$$\langle E \rangle = - \left(\frac{\partial lnZ}{\partial \beta} \right) + \mu_B \langle N \rangle \tag{3.16}$$

$$\langle S \rangle = k_B \frac{\partial T \cdot lnZ}{\partial T} \tag{3.17}$$

$$P_{pressure} = \frac{1}{\beta} \left(\frac{\partial lnZ}{\partial V} \right) \tag{3.18}$$

Where E,S $P_{pressure}$, N, T and k_B are respectively the energy, the entropy, the pressure, the number of particle the temperature and the Boltzmann constant, instead $\beta = \frac{1}{k_B T}$ and Z is the partition function that can be expressed in the following manner

$$lnZ_i(T, V, \mu_i) = \frac{\Delta V g_i}{2\pi^2 \hbar^3} \int_0^\infty \theta_i p^2 \, dp \ln(1 + \theta_i e^{\beta(\mu_i - E)}) \tag{3.19}$$

θ_i is +1 for fermions and -1 for bosons. Global observables such as the particle mean multiplicities can be derived from the previous equation:

$$\langle N \rangle = \frac{\Delta V g_i}{2\pi^2 \hbar^3} \int_0^\infty dp \frac{p^2}{e^{\beta(\mu_i - E)} + \theta_i} \tag{3.20}$$

$$\langle S \rangle = - \sum_K \int_{\Delta V} \int \frac{d^3 x d^3 p}{(2\pi)^3} \left[f_i \ln f_i + \theta_i (1 - \theta_i f_i) ln(1 - \theta_i f_i) \right] \tag{3.21}$$

In this case the distribution is a bit different from the 3.1.

$$f_{i,eq}(x, p) = \frac{g_i}{e^{\beta(\Delta V)(E_i - \mu_i(\Delta V))} + \theta_i} \tag{3.22}$$

can be further developed the by considering the Eq 3.19 Taylor expansion of the logarithmic part, the full derivation is given in the appendix.

$$lnZ_i(T,V,\mu_i) = \frac{\Delta V g_i}{2\pi^2\hbar^3\beta}\sum_K \frac{(\theta_i e^{\beta\mu_i})^k}{k^2}m_i^2 K_2(k\beta m_i) \qquad (3.23)$$

The definition of the chemical potential μ_i is strictly related to the processes at play and to the type of chosen ensemble.it became necessary in order to taking into account the possibility to have fluctuations of the number of particles of species i. This can happen because the volume can exchange particles with its surroundings, incrementing or decrementing the components of each species. This formulation corresponds to the grand-canonical ensemble which is the most commonly used in the description of heavy-ion collisions. For a given species i the chemical potential can be split into $\mu_i = B_i mu_B + S_i\mu_S + Qi\mu_Q$, where B_i , S_i and Q_i are respectively the baryon number, strangeness and electric charge while μ_B , μ_S and μ_Q are the corresponding chemical potentials. For smaller systems, like happen for example in collision between proton or proton and other nucleos, the grand-canonical ensemble is no longer a good description of the system. In this case the volume created after the collision is considerably smaller and it is better to require the local conservation of quantum numbers and so the canonical formulation is more appropriate. it is worth mentioning that the transition from a canonical to a grand-canonical description effectively occurs when the cluster volume is of the order of 100 fm^3 at an energy density of 0.5 GeV/fm^3. If the energy of the collision is not enough the strange quark and antiquark can be non thermalized. So we should add another therm to chemical potential, This term take the form $|s_i|m\bar{u}_s$ where s_i is the total number of strange quarks and antiquarks in hadron and $m\bar{u}_s$ the corresponding potential. However in heavy-ion collisions the s quarks can be fully thermalized. Equation 3.22 is a local thermal and chemical equilibrium distribution function. If the system could be kept at constant volume, any type of strong interaction among the hadrons would leave this distribution unchanged since such microscopic processes again conserve energy, baryon number and strangeness. Instead from a kinematic point of view the equilibrium is not achieved as a result of hadronic rescattering but statistically by interference of many different hadron production channels. The achievement of kinematic equilibrium is due to two different types of processes. The first one is to take the system of hadrons with an arbitrary initial phase-space, that respect the constrain, distribution and let it evolve for a sufficiently long time to obtain the validity of the Eq. 3.22 as a result of the action of elastic and inelastic processes among the hadrons, the kinetic equilibration. Or is possible to realize statistical process which fills hadronic phase-space in the statistically most probable configuration. This is statistical equilibrium. Both processes share the property that they lead to a state of Maximum Entropy. However, statistical hadronization can produce a Maximum Entropy distribution through non-hadronic processes which occur

much faster than any inelastic scattering among hadrons at the given energy and baryon number density.

Starting from measurements of the identified particle yields (dN/dy) in the light flavor sector by using the SHM approach one gains the access to the thermodynamic properties of the system created in the collision. In principle the more particle species are measured the better, in fact all particle that are produced at equilibrium can be used for this purpose. An example of such measurement for different particle species is given in Fig. 3.5. It is possible to see that the large evolution in particle production and identify some key features:

- All particles and their corresponding anti-particles tend to be equally produced if the collision energy is high enough. This is especially true at LHC energies

- Baryons (p and Λ) and mesons (π and K) follow different behaviour with significant baryon/anti-baryon discrepancies at lower energies.

- When μ_B is larger than 0 the baryonic number of the colliding nuclei is to be found in the products of the collision. At low energies, an important fraction of the initial colliding nucleons are found in the final state (large stopping power). For larger beam energies the colliding nuclei become almost transparent to each other (no baryon stopping).

- The production of Λ, similar to p, is affected by the non-zero μ_B at low energies but the effect is reduced since it contains an s quark. At intermediate energies Λ exhibits a decrease similar to that of p.

- At high energies, pions are the most abundant particle species produced

- Particles containing s quarks are subject to a significant increase in their abundances above the SPS energies. This effect known as "strangeness enhancement" was historically identified as a signature typical of the QGP. This aspect will be discuss better later.

- At high energies the production of particles with same mass but different quark content tends to be similar.

The SHM can be used to fit the measured dN/dy using only a limited number of parameters This allows to obtain quantities such as the chemical freeze-out temperature, the system volume V and the chemical potential μ_B. Results Fig. 3.6 show how the best fit parameters to describe the data from Pb–Pb central collisions collected by the ALICE experiment at $\sqrt{s_{NN}} = 2.76$ TeV are: T = 156.5 ± 1.5 MeV, μ_B = 0.7 ± 3.8 MeV, V = 5280 ± 410 fm^3 . The model is able to describe reasonably well measurements of yields which span over 9 order of magnitudes with a $\tilde{\chi}^2 = 1.61$ with a low number of free parameters. The largest tension is observed for p and $\bar{p}$, reaching almost a

3 σ deviation. [**Andronic˙2017**] In addition these results allow for a direct comparison with predictions from lattice QCD. Such comparison is resumed in Fig. 3.7 where is possible to see that the curve is correctly described.

3.0.4   Strangeness and Charmness enhancement

Considering the particles production one would expect a suppression in the production af the heavier flavor with respect to the u and d quark, both for their mass but also for the conservation of quantum number. This is related to the fact that strong interactions conserve the strangeness number exactly. However is known that in microscopic therm the QCD predict that the heavier flavor are produced in pairs. So, ad example, for the small fireball volumes created in elementary particle collisions strange hadron get suppressed since always a second hadron with balancing strangeness has to be created inside the same small volume at the same time, and this requires more energy. More complicated is the problem for the quark u e d because of their similar mass that required he introduction of the isospin. This hold for a canonical formalism. Instead the grand-canonical formulation assumes the average conservation of the quantum number, a condition that is easily reproduced in heavy-ion collisions. For these reason the strangeness suppression is observed in small collision systems such as pp, p $\bar{p}$ and e^+e^-. When quark-gluon plasma disassembles into hadrons in a breakup process, the high availability of strange antiquarks helps to produce antimatter containing multiple strange quarks, which is otherwise rarely made. Similar considerations are at present made for the heavier charm flavor, which is made at the beginning of the collision process in the first interactions and is only abundant in the high-energy environments of CERN's Large Hadron Collider. In addition, the restoration of the chiral symmetry in proximity to the temperature of deconfined transition lowers the constituent mass below ~ 150 MeV thus decreasing the energetic threshold for its production. These reduce the time scale for strangeness saturation and chemical equilibration. The fact that the gran canonical formalism is useful for description of the process tell us that the system behave as if the strange and antistrange hadrons were created independently and statistically distributed over the entire nuclear fireball. This mean that the is not important the initial contrition in witch the pairs $s\bar{s}$ is created for determine the final distribution and make the statistical assumption hold. This point is not completely understood but is probably related to the fact that a significant amount of strangeness diffusion occur before hadronization.

The net strange quark abundance is starting to saturate for temperatures above 160 MeV. This temperature is close to the one of the chemical freeze-out where the relative particle abundances are fixed. As a consequence of the larger amount of strange quarks available before the hadronization it is expected that strange hadrons will be found more abundantly in the final state. The production of strange content in the plasma is predominant with
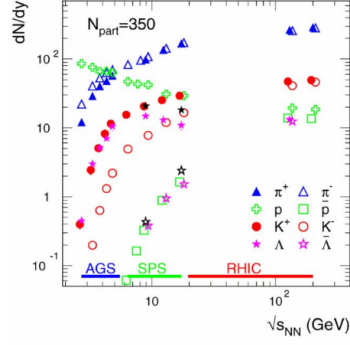
Figure 3.5: The energy dependence of experimenal hadron yields at mid-rapidity for various species produced in central nucleus-nucleus collisions. The energy regimes for various accelerators are marked. Note that, for SPS energies, there are two independent measurements available for the Λ hyperon yields. [**Andronic˙2006**]
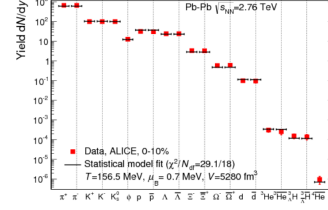
Figure 3.6: adron multiplicities in central (0-10%) Pb–Pb collisions at the LHC, for different particles: $\pi^{\pm}, k^{\pm}, \phi, p, \bar{p}, \Lambda, \bar{\Lambda}, \Xi^{-}, \bar{\Xi}^{+}, \Omega, \bar{\Omega}^{+}, 3^{H}e, 3^{\bar{H}e,3_{H}^{\Lambda}e,3_{\bar{H}e,4\bar{H}e}^{\Lambda}}$ [**Andronic˙2017**]
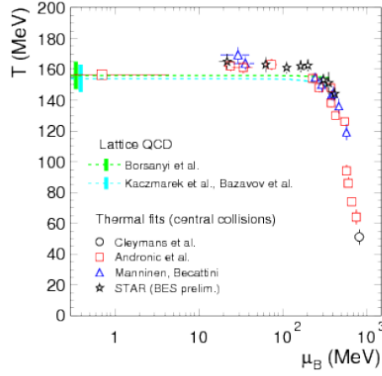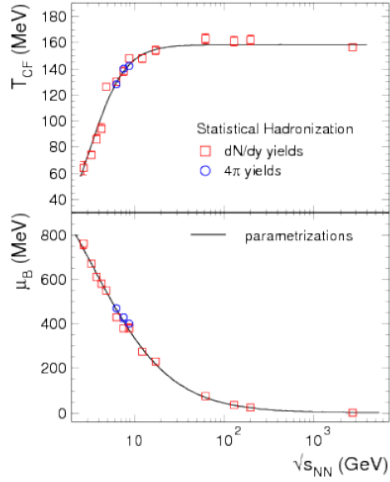
Figure 3.7: The a panel show (a) comparison between the Phase diagram of QCD with data points as obtained at different energies and the thermal model fits from SIS up to LHC data. The panel (b) show the evolution of the temperature of chemical freeze-out and the μ_B as a function of the $\sqrt{s_{NN}}$. [**Andronic˙2017**]

respect to the one formed in interactions occurring after the hadronization phase.

Instead the charm quark mass is much larger than the other described in this section and hence thermal production of charm quarks or hadrons is strongly suppressed. However, with increasing center-of-mass energy the total charm production cross section which results from initial hard collisions increases strongly.

3.0.5   Computer simulation

Using an SHM model we have tried to understand how the production of supernuclei is influenced by different parameter. In particular the focus was on the c-deuteron, a bound state of a Λ_c and a neutron. This choice is related to the fact that this nucleons is the easier to observe in heavy-ion collision due to his mass.

Chapter 4

Y_cN bound state

4.0.1 One Boson exchange model

Before the publications of Hideki Yukawa's papers in 1935 [**yukawa**] physicists cannot explain the results of James Chadwick's atomic model, which consisted of positively charged protons and neutrons packed inside of a small nucleus, with a radius on the order of $10^{-14} - 10^{-15}$ m. This because the electromagnetic forces at these lengths would cause these protons to repel each other and for the nucleus to fall apart. For these reason in 1932, Werner Heisenberg proposed a "Platzwechsel" (migration) interaction between the neutrons and protons inside the nucleus, in which neutrons were composite particles of protons and electrons. These composite neutrons would emit electrons, creating an attractive force with the protons, and then turn into protons themselves [**heisemerg**]. The model just explained violate the linear and anglular momentum and for these reason Enrico Fermi in 1934 proposed the proposed the emission and absorption of two light particles: the neutrino and electron, rather than just the electron. Some month later the soviet physicists Igor Tamm and Dmitri Ivanenko demonstrated that the force associated with the neutrino and electron emission was not strong enough to bind the protons and neutrons in the nucleus.

For these reasons Hideki Yukawa combines both the idea of Heisenberg's short-range force interaction and Fermi's idea of an exchange particle in order to fix the issue of the neutron-proton interaction. For introducing the Yukawa's potential we can start from the Klein-Gordon equation that governs dynamics of free massive scalar, without spin, field

$$\nabla^2 \phi(\vec{r}, t) - \frac{1}{c^2}\frac{\partial^2 \phi(\vec{r}, t)}{\partial^2 t} = \frac{m^2 c^2}{\hbar^2}\phi(\vec{r}, t) \tag{4.1}$$

where ϕ is the wave function, $\vec{r}$ the position, t the time, and m the mass of the particle. In spherical coordinate becomes for the radial component.

$$\frac{1}{r^2}\frac{\partial}{\partial r}(r^2 \frac{\partial}{\partial r}\phi(\vec{r}, t)) - \frac{1}{c^2}\frac{\partial^2 \phi(\vec{r}, t)}{\partial^2 t} = \frac{m^2 c^2}{\hbar^2}\phi(\vec{r}, t) \tag{4.2}$$

A solution for the second equation is.

$$\phi(\vec{r}, t) = -g^2 \hbar c \frac{e^{\frac{i}{\hbar}(\vec{r} \cdot \vec{P} - Et)}}{r} \tag{4.3}$$

Where $\vec{P}$ is the linear momentum and E the energy. For virtual particles hold that $0 \sim p^2 c^2 + m^2 c^4$ so $p \sim \pm imc$ and with the Einsten-De Broglie equation one get that $\lambda = \frac{\pm ih}{mc}$, named Compton wave length, and the solution can be rewritten as

$$\phi(\vec{r}, t) = -g^2 \hbar c \frac{e^{-\frac{r}{\lambda}}}{r} = -g^2 \hbar c \frac{e^{-\frac{rmc}{\hbar}}}{r} \tag{4.4}$$

after have rejectes the divergent solution. The equation 4.4 clarify that massive mediators gives short range interaction. A graphical representation of the phenomena is visible in the pictures, 4.1. Yukawa used his equation aslo to
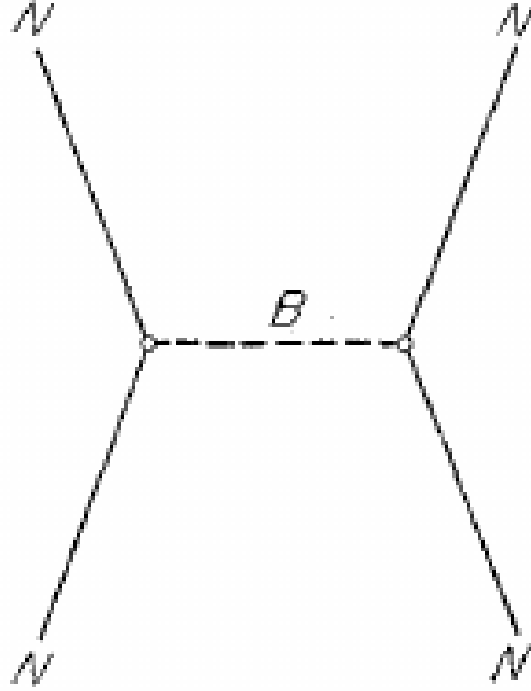

Figure 4.1: The one-boson-exchange diagram of the nucleon-nucleon scattering.

predict the mass of the mediating particle as about 200 times the mass of the electron $\sim$ 140 Mev. Physicists called this particle the "meson," as its mass was in the middle of the leptons and barions. Yukawa's meson was found in 1947, and came to be known as the pion. The model has been referred

to as the "one-boson-exchange model" (OBE model) or the "one-particle-exchange model". This model has presented a new possibility for the realistic understanding of nuclear forces. Basing on the Yukawa potential the Sakata [**sakata**] model was created with the aim of giving a systematic understanding not only of the nucleon-nucleon interaction but of other various strong reactions. In this model, mesons and baryons are considered as composite systems of the fundamental particles: proton (p), neutron (n) and λ-particle (λ), and their antiparticles. With other generalization these works predicted the existence of many resonance levels including the octet mesons now established and seemed to support the basic features of the Sakata model and it became clear from experiment that the wide-spread existence of these resonance levels is one of the fundamental features of the baryon-meson system. From analysis of pion production processes, etc., by the isobar model in which the resonance states are regarded as particles was noted that: The treatment of a resonance as an "elementary" particle has considerable applicability and the non-correlated final states play only a minor role. For these reason the strong interactions should be derived from the fundamental interactions between the fundamental particles, and the Yukawa interaction observed between pion and nucleon is regarded as an effective Hamiltonian which results from the fundamental interactions including all the higher order corrections on the system of composite particles. Higher order effect should not be taken for the Yukawa interaction as because such effects should be considered in the fundamental interaction, not for the model Hamiltonian. Furthermore The Yukawa interaction, as a model Hamiltonian, already contain some of the higher order effects of the fundamental interaction in a certain correlated form. In conclusion we cannot logically exclude the possibility that there may remain some higher order effects of the fundamental interactions not represented by the lowest order diagram and that the higher order of the model interaction might represent such parts. However, we are interested in the OBE model as a zeroth order trial. [**onebosonexchangepotentialmodelapproach**].

4.0.2 Λ_c N interaction

This section is a resume of the [**Charmed-nucleon**] and [**baryonnucleon-potential**] Constructing a model for describe with first-principles analytical calculations of non-perturbative quantum chromo-dynamics (QCD) phenomena is very limited. Furthermore the lack of experimental information on the elementary Y_c N makes the describing of the formation of bound states much more difficult. Thus, the situation can be ameliorated with the use of well constrained models based as much as possible on symmetry principles and analogies with other similar processes, which is still a valid alternative for making progress.

A model was proposed in the early 1990s in an attempt to obtain a simultaneous description of the light baryon spectrum and the nucleon-nucleon interaction [**Valcarce˙2005**]. It was later on generalized to all flavor. In this

model, hadrons are described as clusters of three interacting massive (constituent) quarks. The masses of the quarks are generated by the dynamical breaking of the original $SU(2)_L \otimes SU(2)_R$ chiral symmetry of the QCD Lagrangian at a momentum scale of the order of $\Lambda_c bs = 4\pi f_\pi \sim 1$ GeV, where f_π is the pion electroweak decay constant.

According to Goldstone's theorem, when a continuous symmetry is spontaneously broken, there should be massless particles associated with the broken symmetry. These particles are called Goldstone bosons. In the case of chiral symmetry breaking, the pions are the pseudo-Goldstone bosons. They arise because the chiral symmetry is spontaneously broken, and although they are not strictly massless, they have a very small mass compared to other hadrons like protons and neutrons. [**Smit˙2023**]

Light quarks interact through potentials generated by the exchange of pseudoscalar Goldstone bosons (π) and their chiral partner (σ):

$$V_\chi = V_\sigma(\vec{r_{ij}}) + V_\pi(\vec{r_{ij}}) \tag{4.5}$$

where

$$V_\sigma(\vec{r_{ij}}) = \frac{-g_{ch}^2}{4\pi} \frac{\Lambda^2}{\Lambda^2 - m_\sigma^2} m_\sigma \left[Y(m_\sigma r_{ij} - \frac{\Lambda}{m_\sigma}) Y(\Lambda r_{ij}) \right] \tag{4.6}$$

$$V_\pi(\vec{r_{ij}}) = \frac{g_{ch}^2}{4\pi} \frac{m_\pi^2}{12 m_i m_j} \frac{\Lambda^2}{\Lambda^2 - m_\pi^2} m_\pi \left[Y(m_\pi r_{ij} - \frac{\Lambda^3}{m_\pi^3}) Y(\Lambda r_{ij}) \right] \vec{\sigma_i} \cdot \vec{\sigma_j}$$
$$+ \left[H(m_\pi r_{ij}) - \frac{\Lambda^3}{m_\pi^3} H(\Lambda r_{ij}) \right] S_{ij}^2 (\vec{\tau_i} \cdot \vec{\tau_j}) \tag{4.7}$$

$\frac{g_{ch}^2}{4\pi}$ is the chiral coupling constant, m_i are the masses of the constituent quarks, $\Lambda \sim \Lambda_{CSB}$, $Y(x) = \frac{e^{-x}}{x}$ is the standard Yukawa function, $H(x) = (1 + \frac{3}{x} + \frac{3}{x^2})Y(x)$, $S_{ij} = 3(\vec{\sigma_i} \cdot \hat{r_{ij}})(\vec{\sigma_j} \cdot \hat{r_{ij}})\vec{\sigma_i} \cdot \vec{\sigma_j}$ is the quark tensor operator. Instead perturbative QCD effects are taken into account through the one-gluon-exchange (OGE) potential

$$V_{OGE}(\vec{r_{ij}}) = \frac{a_s}{4} \vec{\lambda_i^c} \cdot \vec{\lambda_j^c} \left[\frac{1}{r_{ij}} - \frac{1}{4}\left(\frac{1}{2m_i^2} + \frac{1}{2m_j^2} + \frac{2\vec{\sigma_i} \cdot \vec{\sigma_j}}{3m_i m_j} \right) \frac{e^{-r_{ij}/r_0}}{r_0^2 r_{ij}} \frac{3S_{ij}}{4m_i m_j r_{ij}^3} \right] \tag{4.8}$$

where $\vec{c}$ are the SU(3) color matrices, $r_0 = \hat{r_0}/\nu$ is a flavor-dependent regularization scaling with the reduced mass ν of the interacting pair, and α_s is the scale-dependent strong coupling constant given by:

$$\alpha_s(\nu) = \frac{\alpha_0}{ln[(\nu^2 + \mu_0^2)/\gamma_0^2]} \tag{4.9}$$

α_0=2.118, μ_0 =36.976 Mev and γ_0=0.113 fm^{-1}. the equation 4.9 give rise $\alpha_s \sim 0.54$ for light quark and $\alpha_s \sim 0.43$ for uc pairs. The table resume all the parameter 4.1

$m_{u,d}$ (MeV)	313	$g_{ch}^2/4\pi$	0.54
m_c (MeV)	1752	$m_\sigma\,(fm^{-1})$	3.42
$\hat{r}_0$ (MeV fm)	28.170	$m_\pi\,(fm^{-1})$	0.70
$\mu_c\,(fm^{-1})$	0.70	$\Lambda\,(fm^{-1})$	4.2
b (fm)	0.518	a_c (MeV)	230

Table 4.1: The table summarizes the typical values of the parameters present in the previous equation.

Finally, any model imitating QCD should incorporate confinement. Although it is a very important term from the spectroscopic point of view, it is negligible for the hadron-hadron interaction. Lattice QCD calculations suggest a screening effect on the potential when increasing the interquark distance which is modeled here by.

$$V_{CON}(\vec{r_{ij}}) = -\alpha_c(1 - e^{-\mu_c r_{ij}})\vec{\lambda}_i^c \cdot \vec{\lambda}_j^c \tag{4.10}$$

The figures 4.1 shows the different diagrams contributing to the charmed baryon-nucleon interaction. The first type of interaction, visible in (a) and (b), is mediated by the exchange of a boson between light quark or between a light ad heavy flavor. The second one instead take in account also the exchange of the identical light quark (c) and (d). The second possibility correspond to short range that contain one-gluon exchange contributions that are also missed in hadronic models.
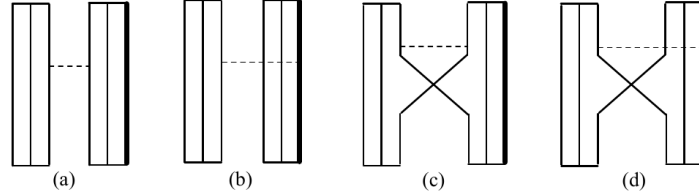

Figure 4.2: The vertical solid lines represent a light quark, u or d. The vertical thick solid lines represent the charm quark. The dotted horizontal lines stand for the exchanged boson. (a) Interaction between two light quarks. (b) Interaction between the heavy and a light quark. (c) Interaction between two light quarks together with the exchange of identical light quarks. (d) Interaction between the heavy and a light quark together with the exchange of identical light quarks.

A numerical simulation of the potential is described in **??** performed with lattice QCD with lattice spacing a =0.0907(13)fm and a physical lattice size of La=2.902(42)fm. In order to see the quark mass dependence of the potentials, the members of the study had employed three ensembles of gauge configurations. The hopping parameters of these ensembles are κ_{ud} =0.13700 (Ensemble 1), 0.13727 (Ensemble 2), 0.13754 (Ensemble 3) for u, d-quarks. The figure 4.3 show the λ_cN central potential in the 1_0^S channel for each ensemble with different mass considered for the pion. For Ensemble 1 $m_\pi \sim$ 700 Mev, $m_\pi \sim$ 570 Mev for Ensemble 2 and 410 Mev for Ensemble 3. They found a repulsive core at short distances (r ¡ 0.5 fm) and an attractive one for intermediate distances (0.5 ¡ r ¡ 1.5 fm). They discovered also that the

Figure 4.3: The figure show Λ_cN central potential in the 1_0^S channel for each ensemble. The potential is calculated for $m_\pi \approx 700$ MeV case (Blue), for $m_\pi \approx 570$ MeV case (Green) and for $m_\pi \approx 410$ MeV case (Red).
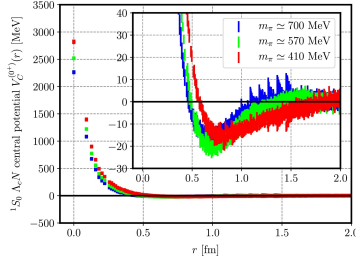
Figure 4.4: The figure show Λ_cN central potential in the 3_0^S channel for each ensemble. The potential is calculated for $m_\pi \approx 700$ MeV case (Blue), for $m_\pi \approx 570$ MeV case (Green) and for $m_\pi \approx 410$ MeV case (Red).
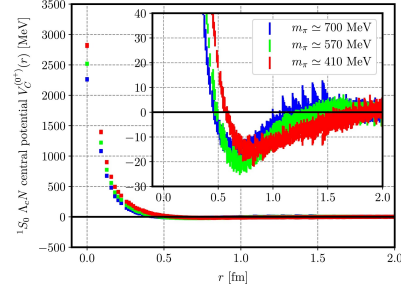
height of the repulsive core increases and the minimum of the attractive pocket shifts outward, as u, d quark masses decrease. A variation of the repulsive core against u, d quark masses may be explained by the fact that the colour magnetic interaction is proportional to the inverse of the constituent quark mass. The same operation has also be done with a Λ_cN system with $J^P = 1^+$ obtaining the result visible in figure 4.4, the result is similar to the one in 1_0^S channel exept at short distance (r¡0.5fm) but in both cases the actrattive potential is weaker than the Λ_cN system.

The weaker potential than Λ_CN could be explained from following facts:

- The long-range contribution is expected to be caused by the K meson exchange for ΛN interaction. In the system, however, the K meson (strange quark) exchange is replaced by the D meson (charm quark) exchange, and this contribution is highly suppressed due to the much heavier D meson mass than the K meson mass.

- The one-pion exchange in the transition is considered to give a sizable contribution to the effective ΛN interaction. In the system, however, this contribution is expected to be suppressed due to the large mass difference between Λ_cN and Σ_cN

If no meson exchanges were considered, the S wave phase shifts of the Λ_CN system are very similar to the corresponding NN scattering. In both partial waves one obtains typical hard-core phase shifts due to the short-range gluon and quark-exchange dynamics. However,the hard-core radius in the spin-singlet state is larger than in the spin-triplet one leading to a more attractive interaction in the spin-triplet partial wave due to a lower short-range repulsion. In fact, the hard cores caused by the color magnetic part of the OGE potential have been calculated obtaining 0.35 fm for the spin-triplet state and 0.44 fm for the spin-singlet one.

4.0.3 Potential energy

4.0.4 Possible Λ_c supernuclei

One of the most interesting applications of the charmed baryon-nucleon interaction is the study of the possible existence of charmed hypernuclei. Since the Λ_c interaction is dominated by the spin-independent central force, as we discussed in the previous section, the spectrum of hypernuclei, if they exist, would probably can be approximated by the following single-folding potential defined by

$$V_f(\vec{r}) = \int d^3 f' \rho_A(\vec{r}') V_{\Lambda_c N}(\vec{r} - \vec{r}') \qquad (4.11)$$

where $\rho_A(\vec{r})$ correspond to ne nuclear density corresponding with the atomic number A and $V_{\Lambda_c N}$ stands for the two body spin-independent central potential of the Λ_c system. The study described assumed,

$$\rho_A(\vec{r}) = \rho_0 \left[1 + e^{\frac{r-c}{a}} \right] \qquad (4.12)$$

where the parameters employed ρ_0, c, a are the same used for described spherical nuclei. They test the equation with different set of parameter taking the value assumed in the following nuclei 12^C, $28^S i$, $40^C a$, $58^N i$ and $208^P b$. With the following potential they calculate the binding energy for Λ_c hypernuclei by the Gaussian expansion method. The result is shown in figure 4.5. As expected the binding increases as the atomic number increases. Furthermore, as the potential approaches to the physical one (as the u, d quark masses decrease toward physical values), the binding energy increases. These results suggest that hypernuclei may exist, if their binding energy is larger than the Coulomb repulsion energy described by**??**.

It's interesting to confront energy expectation taking into account also the Culomb repulsion, the result is reported in figure 4.6. It's possible to see that only the system with lower atomic number could eventually exist.

The binding energy of Λ_c hypernuclei has been analyzed in **??** using the HAL QCD for $m_\pi = 410$ MeV.
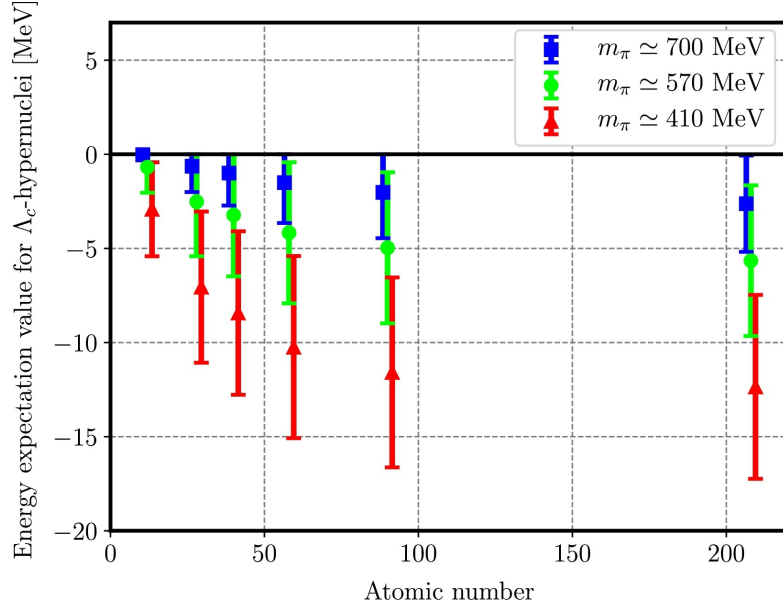
Figure 4.5: The figure show the binding energy in symmetric nuclei with the parameter assumed for each atomic number for each ensemble. The binding energies are calculated from the folding potentials for Λ_c hypernuclei by using the Gaussian expansion method. The folding potentials are constructed from the spin-independent central potential of the Λ_cN system

Figure 4.6: The figure show the expectation value of folding potential for Coulomb force in Λ_c hypernuclei (Blue). The expectation values are calculated from the binding solution of the Λ_c hypernuclei for Ensemble 3 ($m_\pi \approx 410$ MeV). For comparison, the binding energy of Λ_c hypernuclei (Green) and sum of them (Red) are also plotted.

Chapter 5

ALICE

The A Large Ion Collider Experiment (ALICE) is a detector designed for heavy-ion physics at the Large Hadron Collider (LHC). It is primarily used to study lead-lead collision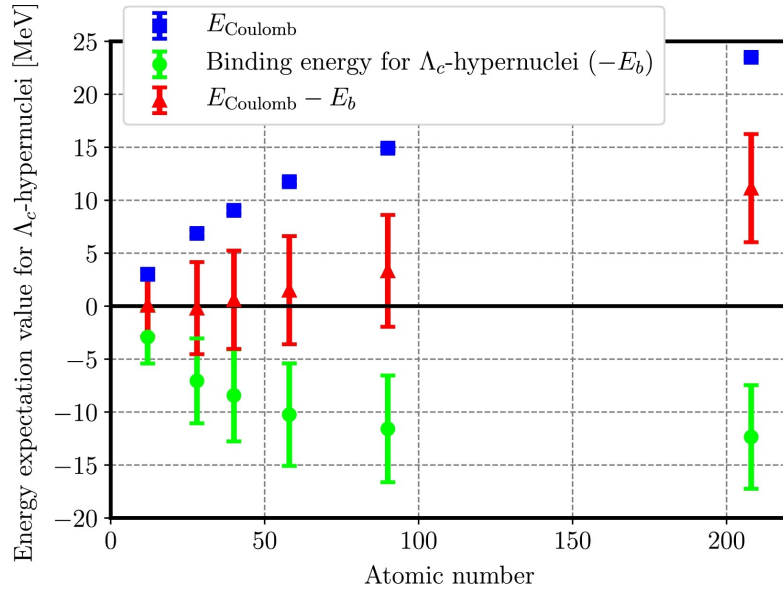s, recreating conditions similar to those just after the Big Bang. These extreme conditions may also be present in neutron stars and other astrophysical objects. The goal of ALICE is to recreate and study quark-gluon plasma. This is crucial for the understanding of the formation and evolution of quark-gluon plasma, the mechanisms that confine quarks and gluons, and the nature of the strong nuclear force. This force plays a key role in generating the bulk of the mass of ordinary matter. ALICE also investigates phenomena such as quark confinement and chiral symmetry restoration, which are important for understanding the fundamental behavior of matter at the smallest scales. The ALICE collaboration uses the 10 000-tonne ALICE detector 26 m long, 16 m high, and 16 m wide to study quark-gluon plasma. The detector sits in a vast cavern 56 m below ground close to the village of St Genis-Pouilly in France, receiving beams from the LHC. [**Alice**] The lead isotope used in LHC is ^{208}Pb. The lead is taken from lead vapor obtained heating the substance and then with a electrons are stripped with electric current.

The ALICE sub-detectors are categorized into three main groups: one at mid-rapidity $|\eta|$ ¡1, the central barrel, and one at forward rapidity -4 < $\eta < -2.5$, and the the muon spectrometer dedicated to muon identification. However the muon spectrometer is included in the forward detectors. The apparatus scheme can be resumed in the following manner.

- The central barrel detectors can measure all over the azimuthal angle and include in order from the interaction point and going outward:

  1. The Inner Tracking System (ITS) is a silicon tracking system composed of six cylin- drical layers. its main goal is to identify the position of the primary vertex with a resolution better than 100 μm and provide tracking of charged particles. of charged particles down to

2. the Time Projection Chamber (TPC) is used for charged particle identification.

3. the Transition Radiation Detector (TRD) is composed of different gas chamber and radiation for identify and track electrons

4. the Time of Flight (TOF) measure the time of flight providing important information for particle identification and a dedicated trigger for cosmic ray events and Ultra Peripheral Collision collisions (UPC).

These subsystem are mostly dedicated to vertex reconstruction, tracking, particle identification and momentum measurement. Are also present some specialized detectors with limited acceptance.

1. High-Momentum Particle Identification Detector (HMPID) is used for study Cherenkov phons for identify particle with $p_\perp$ ¿ 1 GeV/c

2. PHOton Spectrometer (PHOS), is an electromagnetic calorimeter used for photons identification and as high-energy photon trigger.

3. ElectroMagnetic CaLorimeter (EMCal) is a Pb-scintillator calorimeter for identify photons and pion with η¿0.7 and is also used as jet trigger.

4. Di-jet Calorimeter (DCal).

- The forward detector include:

1. Muon spectrometer for reconstruct heavy quark hadrons thought their weak decay in the channel $\mu^-\bar{\nu}_\mu$ or $\mu^+\nu_\mu$ or for electrodynamical decay in the couple $\mu^+\mu^-$

2. Forward Multiplicity Detector (FMD) composed by several layers of silicon strip detectors at a distance of 70÷150 cm from the interaction point.

3. Photon Multiplicity Detector (PMD)

4. Zero Degree Calorimeters (ZDC) a proton and neutron calorimeter

5. V0 Detectors

6. T0 detectors

[**Padhan:2924203**] [**Arata:2922803**]

In the following section we will discuss some of the most important one.

5.0.1 Inner Tracking System (ITS)

The Inner Tracking System (ITS) is a crucial part of the ALICE tracking system, positioned as the innermost sub-detector of the central barrel, closest to the beam pipe and the interaction point. It consists of six concentric

cylindrical layers of silicon detectors, comprising two layers each of Silicon Pixel Detector (SPD), Silicon Drift Detector (SDD), and Silicon Strip Detector (SSD). The ITS covers the pseudorapidity region —η— ¡ 0.9 for interactions occurring within 10 cm from the detector center. The two innermost
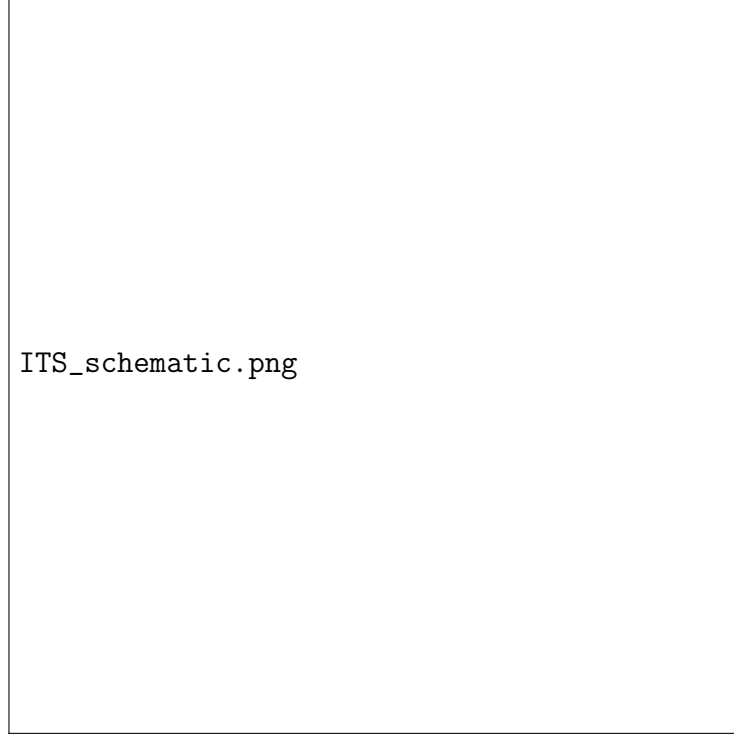

Figure 5.1: Schematic diagram of the Inner Tracking System (ITS) of the ALICE experiment.

layers are constructed using Silicon Pixel Detectors (SPD), located at radial distances of 3.9 cm and 7.6 cm from the beam pipe. These layers cover extended pseudorapidity ranges of —η— ¡ 2.0 and —η— ¡ 1.4, respectively. They consist of hybrid silicon pixel detectors, totaling 9.810^6, which generate binary signals upon interaction with charged particles, facilitating particle counting. The primary functions of the SPD are to determine the position of the primary vertex with a high resolution, surpassing 100 μm, to help isolate events coming from pileup, and to contribute to the triggering system due to their fast response. The SPD also ensures the accurate determination of track multiplicity and contributes to achieving an impact-parameter resolution surpassing 50 μm for tracks with transverse momentum $p_\perp$ ¿ 1.3 GeV/c. The two intermediate layers are the Silicon Drift Detector (SDD), situated at radii of 15.0 cm and 23.9 cm, covering —η— ¡ 0.9. The SDD has very good multi-track capability and provides two out of the four measurements of specific dE/dx employed for PID by the ITS. It provides two-dimensional spatial information (r ϕ and z) with a spatial resolution of 35 μm (r ϕ) and 25 μm (z). The SDD determines particle positions using drift time estimation and charge centroid measurement and is structured with a central cathode

for precise particle tracking. The two outermost layers employ double-sided Silicon Strip Detectors (SSD), located at radial distances of 38.0 cm and 43.0 cm, covering —η— ¡ 1.0. The SSD is essential for the prolongation of tracks from the main tracking detector of ALICE, the Time Projection Chamber (TPC), to the ITS. It provides a spatial resolution of 20 μm (r ϕ) and 830 μm (z) and 27 μm (r ϕ) and 830 μm (z) according to the third source, with a fast readout time of 1 μs. Besides connecting tracks, the SSD also provides dE/dx information, enabling the ITS with the standalone capability to serve as a low-pT particle spectrometer. Each SSD module consists of a 1536-strip double-sided sensor connected to twelve front-end chips that furnish position and energy deposition details. The primary responsibilities of the ITS include:

- Reconstructing the primary vertex of collisions with a high resolution, surpassing 100 μm

- Reconstructing the secondary vertices, points of decay for short-lived hadrons

- Particle identification (PID) and tracking of low-momentum particles with momentum below 200 MeV/c.

The ITS can also perform "standalone" tracking that reconstructs charged particles in the low pT region (e.g., pions with pT ¡ 80 MeV/c) by using exclusively the information from its six planes. The high granularity of ITS allows maintaining the detector occupancy below a safe level. The good resolution of the detector allows to separate primary and secondary vertices from weak decays, hyperons, D and B mesons. The analogue readout in the four outer layers (SDD and SSD) samples the particle energy loss (dE/dx) in the material, providing information sufficient to perform PID below 700 MeV/c. [**Padhan:2924203**] [**amsdottorato9036**] [**Cheng:2908766**] [**Arata:2922803**]

5.0.2 Time projection chamber (TPC)

is the main tracking detector of the central barrel. It is specifically designed for measure tracks with transverse momentum range 0.1 Gev/c $\div$ 100 Gev/c and pseudorapidity range $|\eta|$ ¡0.9. It is positioned at radial distances ranging from 85 to 247 cm from the beam pipe, extending along the beam direction with a total length of 510 cm. It is divided along the beam axis into two equally large drift regions by a central cathode, each having a length of 2.5 m. On the opposite sides of the central electrodes is the readout, which is equipped with multi-wire proportional chambers (MWPC). Each of the 18 readout chambers covers an azimuth of 20°. The grand-total span along the beam direction is of 500 cm. The total volume of TPC ($\sim$ 90 m^3) can be filled with different gases depending on the running conditions. The perfect candidate are gas with a small radiation length and low multiple scattering rates, usually is filled with a mixture containing different combination of argon,

neon. carbon dioxide and sometimes nitrogen. When charged particle traverse the gas ionize him and creating electron-ion pair. These ionization electrons then drift towards sensing electrodes under a uniform electric field, typically achieved by applying a high voltage of around 100 kV between the central electrode and the readout plates. The ionization electrons drift with a speed of approximately 2.7 cm/s, corresponding to a maximum drift time of around 92 ms. This drift process allows for the spatial localization of the ionization event along the particle's trajectory. Additionally, the presence of a uniform magnetic field of 0.5 Tesla along the z-direction causes charged particles to bend in curved paths. It enables precise momentum measurements based on the curvature of the trajectories. The position resolution for the inner/outer radii ranges from 800 to 1100 μm in the transverse plane (r ϕ) and from 1100 to 1250 μm along the beam axis (z). The total charge collected at the end plates for each track is proportional to the particle energy loss in the gas. This allows a sampling of the dE/dx and therefore perform PID below 1 GeV/c and above 3 GeV/c. The resolution on the dE/dx is 5% for isolated tracks (low multiplicity collisions), while the number of particles increase such as Pb–Pb collisions (high multiplicity collisions), the resolution is 7%. This is due to the increased probability to have hits close in space. In addition, the contribution of positive ions to the signal shape increases with the particle occupancy. An other effect is due to the formation of large amount of charged particles that can induce local modifications to the external electric field modifying the drift speed and complicating the reconstruction of the track. It can also be use for identify particle thanks to the measure of dE/dx as they traverse the gas volume. The specific energy loss can be described by the Bethe-Bloch formula, which depends on the particle species and it momentum, and the properties of the traversed medium, The energy loss can be estimate in the following manner proposed by [**Rolandi:2008ujz**].

$$f(\beta) = \frac{P_1}{\beta^{P_4}} \left(P_2 - \beta^{P_4} - ln(P_3) \frac{1}{(\beta\gamma)^{P_5}} \right) \qquad (5.1)$$

Where β is the particle velocity in c unit, γ the Lorentz factor, P_{1-5} free parameter that must be estimate from data.

5.0.3 Time Of Flight (TOF)

The Time Of Flight (TOF) detector is a large array of Multi-gap Resistive-Plate Chambers (MRPC), located at 3.7 m and 3.99 m radial distance, respectively, from the interaction point. It is designed to identify charged particle produced in pseudorapidity of —η— ¡ 0.9 and with an intermediate momentum range (0.5 ¡ $p_\perp$ ¡ 4 GeV/c). In addition TOF has been used to provide a trigger specific for cosmic ray and UPC events. The TOF detector has a modular structure divided along the azimuthal direction into 18 super modules, each one segmented into 5 modules along the z axis as visible in Fig **??**.

In total there are 1593 Multi-Gap Resistive Plate Chamber (MRPC) strip detectors organized each one divided into two rows of 48 pickup pads, a total of 96 pads per strip and 152 928 readout channels. If a particle ionizes the gas in the detector, an avalanche process will be triggered to generate signal on the readout electrodes. The total signal is the analogue sum of signals from many gaps and the time resolution is about 40 ps with a detector efficiency of close to 100%. Particle identification is performed by combining the information bring by the linear momentum module (p) and track length (l) with the measurement of the time of flight (t) in TOF. The mass (m) corresponding to the one of the detected particle can be obtained.

$$p = m\gamma\beta c \longleftrightarrow m = \frac{p\sqrt{1-\beta^2}}{c\beta} = \frac{p\sqrt{\frac{1}{\beta^2}-1}}{c} \tag{5.2}$$

The β parameter can be measured in the following manner

$$\beta = \frac{v}{c} = \frac{l}{c\,t} \tag{5.3}$$

So

$$m = \frac{p\sqrt{\left(\frac{t}{lc}\right)^2 - 1}}{c} \tag{5.4}$$

The relative uncertainties can be estimated assuming that the variable ar not correlate in the following manner assuming c=1.

$$\frac{\sigma_m}{m} = \sqrt{\left(\frac{\sigma_p}{p}\right)^2 + \left(\left(\frac{\sigma_t}{t}\right)^2 + \left(\frac{\sigma_l}{l}\right)^2\right)\left(\frac{E}{m}\right)^4} \tag{5.5}$$

The proof is in the appendix. Studying the equation became clear that, at large momenta, the resolution on the track momentum (σ_p) becomes negligible and the total uncertainty is driven by precision on the timing (σ_t) and track length (σ_l). For these reason the TOF detector was designed to achieve a timing resolution better than 90 ps. [**Padhan:2924203**] [**amsdottorato9036**] [**Cheng:2908766**]

5.0.4 Central Barrel Detectors

Transition Radiation Detector (TRD)

The Transition Radiation Detector (TRD) is ositioned between the TPC and TOF detector, it covers a pseudorapidity range of —η— ¡ 0.84. It consist in a total of 522 detectors divided into 18 super modules in the azimuthal direction, each super module contains 30 modules arranged in 5 stacks along the beam axis, with each stack further arranged in 6 layers. This configuration results in approximately 1.15 million readout channels. It is principally use for electron

identification in hight momentum region (p ¿ 1 GeV) where discriminating between electrons and pions using traditional dE/dx techniques becomes challenging and triggering processes within particle collision experiments. When charged the particles try to transverse the detector flows through two media with different dielectric constants and emits transition radiation. The emitted radiation proportional to the Lorentz factor of the particle. Since different particles have different masses and velocities, they emit varying amounts of transition radiation that alow us in the identification. [**Padhan:2924203**] [**amsdottorato9036**]

Photon Spectrometer (PHOS)

The Photon Spectrometer (PHOS) it's an electromagnetic calorimeter known for its high spatial and energy resolution. Positioned on the outer region of the TOF detector. PHOS covers a pseudo-rapidity range of 0.12 ¡ η ¡ 0.12 and provides coverage of 70 in the azimuthal direction using scintillating material called Lead Tungstate ($PbWO_4$). With a dynamic energy range of 0.1 GeV to 100 GeV. Its main goal is to measure QGP temperature, and space-time dimensions, and study deconfinement through jet quenching. [**Padhan:2924203**] [**amsdottorato9036**]

High-Momentum Particle Identification Detector (HMPID)

The High Momentum Particle Identification Detector (HMPID) is a low-acceptance detector. It covers $\sim 11m^2$ corresponding to 5% of the total central barrel acceptance. Is dedicated to the identification of charged hadrons with $p_\perp$ ¿ 1 GeV/c, thus extending the PID capabilities of the ITS, TPC and TOF at high momentum. It cover a pseudorapidity range of -0.6 ¡ η ¡ 0.6. It consist mainly of two parts: the radiator and the photon detector. Comprising seven Ring Imaging Cherenkov (RICH) counters. [**Padhan:2924203**] [**amsdottorato9036**]

Electromagnetic Calorimeter (EMCaL)

The EMCal is composed of towers of $6 \times 6 \times 20$ cm^3 each one constituted of 76 alteranating layers of lead and scintillator (not uniform in contrast to PHOS); it was designed for the measurements of electrons from heavy-flavor hadron decays but not only. It also identifies high-energy particles. In addition it can enhances energy resolution across various momenta, enabling precise measurements of jet quenching. The electromagnetic component of jets, spectra of direct photons and neutral mesons and correlations of those photons with hadrons or jets. It has been completed by the DCal, at the opposite side of the beam. Both calorimeters are trigger detectors and they select collisions when there is a high energy deposition, typically a few GeV. [**Padhan:2924203**] [**Arata:2922803**]

5.0.5 Forward Detectors

VZERO detector (V0)

The V0 detector consists of two circular arrays of scintillator counters (named V0A and V0C) one per side with respect to the interaction point. They are positioned asymmetrically on both sides of the interaction point. The V0A covers the pseudorapidity region 2.8 ¡ η ¡ 5.1 while V0C -3.7 ¡ η ¡ -1.7. They are important both in pp collision and AA collision for the following reason;

- Triggering: The V0 detector provides a minimum bias trigger signal. This is important because help us to detect a broad range of inelastic collision events without introducing significant selection bias.

- Vertex determination: The VZERO detector succeed the rejection of background events generated due to the interaction of beams with residual gas within the beam pipe and with mechanical structures along the beamline. It is possible thanks to the time gap between signals from V0A and V0C.

- Centrality determination: The signal given by the V0 detector is proportional to the number of particles traversing it. So, using the signal aptitude, it can be used for the multiplicity/centrality determination. This information are precious for for understanding the collision geometry and interpreting experimental results accurately.

[**Padhan:2924203**] [**amsdottorato9036**]

T0 Detectors

The T0 detector consists of two arrays, T0A and T0C, of Cherenkov counters placed along the beam pipe on each side of the interaction point, respectively at -72.7 cm and 375 cm. The pseudorapidity coverage are 4.61 ¡ η ¡ 4.92 (T0A) and -3.28 ¡ η ¡ -2.97 (T0C). Its primary function is to provide a fast timing signal for the TOF detector, serving as a collision time reference. It can be also use for an independent determination of the vertex position along the beam axis (with a precision of ± 1.5 cm). [**Padhan:2924203**] [**amsdottorato9036**]

Zero Degree Calorimeter (ZDC)

The Zero Degree Calorimeter (ZDC) consists of four calorimeters, two for protons (brass-quartz proton ZP) and two for neutrons (tungsten-quartz neutron ZN), on each side. located at $\sim$ 112.5 cm away from the Interaction Point, symmetrically in both directions. ZDC measures the energy of spectator nucleons, assisting in centrality estimation and luminosity detection in heavy-ion collisions. By determining collision geometry and overlap regions of colliding nuclei, and estimating the number of participant nucleons.[**Padhan:2924203**] [**amsdottorato9036**]

Muon Spectrometer

The muon spectrometer is located 14 m in the negative beam direction, with a pseudorapidity range of 4 ¡ η ¡ 2.5 and the resonances can be detected down to zero transverse momentum. It help to studies the complete spectrum of heavy quarkonia via their decay in the $\mu^+\mu^-$ channel. It is made of carbon and concrete in order to limit the multiple scattering and the energy loss of the muons. The inner beam shield protects the chambers from background originating from particles at small angles. It is made of tungsten, lead and stainless steel to minimize the background arising from primary particles emitted in the collision and from their showers produced in the beam pipe and in the shield itself. The 4 planes of RPCs (Resistive Plate Chambers) arranged in 2 stations and positioned behind a passive muon filter provide the transverse momentum of each μ. The spatial resolution should be better than 1 cm. Special front-end electronics have been designed to obtain the time resolution of 2 ns necessary for the identification of the bunch crossing. The dipole magnet is positioned at about 7 m from the interaction providing a magnetic field nominally of B = 0.7 T but can be changed by the requirements on the mass resolution. [**Padhan:2924203**] [**Alicemuonspectometer**]

5.0.6   Track and vertex reconstruction

The purpose of tracking algorithms [**Cheng:2908766**] is to use the the cluster information transforming them into track information, obtaining the best possible approximation of the real trajectory of the particles crossing the detector. process that uses the Kalman filter algorithm to accurately determine the trajectory of particles as they pass through the detector layers. The tracking procedure starts with the clusterization step. Starting from the collected raw data, from each detector, the data cluster are produced. The cluster correspond to groups of hits produced by a single particle interaction with a detector element and contain his positions, signal amplitude, signal times, and their associated errors. The clusterization is performed separately for each detector. The reconstruction of the primary vertex is an essential step, as it is referred to the interaction point. Usually, each collision event only involves one primary interaction point, and numerous tracks traverse the detectors. In this ambitious the information provided by the SPD detector plays a crucial role in establishing a preliminary interaction vertex. This is the space point that minimises the distance among the tracklets, which are the track segments reconstructed by associating pairs of clusters in the two SPD layers. So is possible to localize the vertex searching the point where most of the tracklets converge. In high multiplicity events the algorithm is repeated several times, discarding at each iteration those clusters which contributed to already found vertices. The tracking algorithm can be separated into two steps: the track finding and the track fitting. For the track finding, two methods are used. The first one is called Linear Track Finder (LTF) and it looks for cluster position

aligned along a straight line. However the magnetic field curve the trajectory of charged particle but the deviation can be neglected at least at hight $p_\perp$ hence supporting the choice of a LTF for such tracks. For help in these work a radial tolerance Rcut is given, a graphical resume is visible in Fig **??** . If a track had been recognized in the previous step the correspondent cluster are removed from the list of available clusters considered in the further steps. The next step consist on a Cellular Automaton (CA) approach particularly suited for low-momentum tracks, sensitive to multiple scatterings. It is based on a propagation and joining of "segments". A segment is a portion of line connecting two clusters from two consecutive disks: So starting from a given segment, considered as the first, the algorithm search the further one towards imposing track continuity conditions. Tracks are only accepted if they have at least 20 associated clusters (out of a possible 159) and have missed fewer than 50% of the expected clusters. Only after that the track candidates are found a track fitting algorithm is applied in order to extract the kinematic parameters of each track. It is able to determine the spatial and momentum coordinates considering material effects, updates the parameters based on measurement. The process is repeated for each track cluster [**Herrmann:2920632**].

The efficiency of the track reconstruction process is influenced by the transverse momentum of the tracks. Efficiency drops below $p_\perp$ ¡ 0.5 GeV/c, as visible in Fig **??** due to energy loss in the detector material, while higher $p_\perp$ tracks, which are typically straighter, may encounter reduced efficiency in areas where clusters are lost due to dead zones between readout sectors. [**Padhan:2924203**].

More specifically for primary vertex finding the most useful instrument is the SPD. It is ideal for fast vertex measurements as it provides a quick response, also because is closest to the interaction point, and has excellent transverse plane resolution due to its high granularity. The resolution of the SPD Vertex is of 10 μm in Pb–Pb collisions and 150 μm in pp collisions at $\sqrt{s_{NN}} = 7$ TeV. In ALICE, three primary algorithms are used for vertex reconstruction

- VertexerSPDz: Provides the measurement of the z-coordinate of the interaction point using the SPD. It calculates the z-coordinate from tracklets correlations in the SPD layers and iteratively refines the estimate by focusing on the peak of the z-distribution.

- VertexerSPD3D: Offers a three-dimensional measurement of the primary vertex using the SPD tracklets. To perform the task it minimize the distances among tracklets.

- VertexerTracks: Provides a three-dimensional measurement of the primary vertex using reconstructed tracks. Where the final vertex position and its covariance matrix are obtained through a fitting process.

[**Padhan:2924203**] Once the tracks and the interaction vertex have been found in the course of event reconstruction, a search for photon conversions and secondary vertices from particle decays is performed. Instead the hadronic interaction vertices are found at the analysis level by identifying groups of two or more tracks originating from a common secondary vertex with precises restriction in the invariant mass of the pair. In ALICE, secondary vertex reconstruction begins by selecting tracks with Distance of Closest Approach DCA greater than 0.5 mm in pp collisions or 1 mm in Pb–Pb collisions. A graphical resume is visible in Fig **??**. For each pair of selected tracks with opposite charges, known as V^0 candidates, are then subjected to further selection criteria:

1. The distance between the two tracks at their PCA is requested to be less than 1.5 cm

2. The PCA is requested to be closer to the interaction vertex than the innermost hit of either of the two tracks.

3. The cosine of the angle between the total momentum vector of the pair and the line connecting the primary and secondary vertices must be greater than 0.9

For V^0 candidates with a momentum below 1.5 GeV/c the cut are relaxed. The reconstruction of more complex secondary vertices is performed later, at the analysis stage. For the study of heavy-flavor decays close to the interaction point, the secondary vertex is searched starting from point that satisfied other different topological condition. [**ALICE:2014sbx**]

5.0.7   centrality

An important parameter to characterize heavy-ion collisions is the centrality, which is an observable related to the transverse distance b between the centers of the colliding nuclei. Is expressed in therm of the fraction of the total hadronic cross section σ_{AA}. The centrality percentile of collisions with impact parameter ranging in the interval $[b_1, b_2]$ is given by

$$c(b_1, b_2) = \frac{\int_{b_1}^{b_2} db \frac{d\sigma}{db}}{\int_0^\infty db \frac{d\sigma}{db}} = \frac{\int_{b_1}^{b_2} db \frac{d\sigma}{db}}{\sigma_{AA}} \tag{5.6}$$

The collisions with the smallest b are called central collisions, and the collisions with large b are called peripheral collisions. The centrality has important consequence in the particle abundances expected, in particular in the number of the charged one. This observable is frequently used and is called multiplicity, defined as the total number of charged particles produced in a collision. For these reason the centrality can be obtain experimentally starting from the measure of the multiplicity or by counting the number of spectator nucleons,

the nucleons that non interact during the collision. so if N_{ev} is the number of collision and N_{ch} the number of charge particle the centrality can be expressed as

$$c(b_1, b_2) \approx \frac{1}{N_{EV}} \int_{N_{ch\ 1}}^{N_{ch\ 2}} dN_{ch} \frac{dN_{ev}}{dN_{ch}} \tag{5.7}$$

In ALICE the centrality determination is usually determined by using the sum of the signals amplitudes in the V0 detector (V0A and V0C) or in the ZDC. In general the probability for a collision to happen at a given impact parameter b can be computed as

$$P(b) = \sigma_{NN} T_{AA}(b) \tag{5.8}$$

Where σ_{NN} is the cross section and T_{AA} is the nuclear overlapping function, it can be computed from the single nucleon distribution of the interacting nuclei. It' possible to imagine this parameter as probability to have a nucleon at the same position in the transverse plane in both colliding nuclei. The centrality of each collision has to be determined experimentally in order identify peculiar behaviour that can arise for very specific centrality classes. [**amsdottorato9036**]

5.0.8   Particle identification

Chapter 6

Appendix

.0.1 Cooper-Frye

We start with the proof that $dy p_\perp dp_\perp d\phi_p = dy m_\perp dm_\perp d\phi_p$, in fact $m_\perp = \sqrt{m^2 + p_\perp^2}$ so $\frac{dm_\perp}{dp_\perp} = \frac{p_\perp}{\sqrt{m^2 + p_\perp^2}} = \frac{p_\perp}{m_\perp}$ and the result follow immediately.

For the other equation starting from 3.4 and inserting 3.1 one get

$$
\begin{aligned}
\frac{dN_i}{dy\, m_\perp\, dm_\perp\, d\phi_p} &= \frac{g_i}{(2\pi)^3} \sum_{n=1}^{\infty} (\pm)^n \int d^2 r_\perp\, \tau_f\, e^{n\mu_i/T} e^{n\gamma_\perp \vec{v_\perp} \cdot \vec{p_\perp}} \\
&\qquad \int_{-\infty}^{+\infty} d\eta\, (m_\perp \cosh(y-\eta) - \vec{p}_\perp \cdot \nabla_\perp \tau_f)\, e^{-n\gamma_\perp m_\perp \cosh(y-\eta)/T} \\
&= \frac{g_i}{(2\pi)^3} \sum_{n=1}^{\infty} (\pm)^n \int d^2 r_\perp\, \tau_f\, e^{n\mu_i/T} e^{n\gamma_\perp \vec{v_\perp} \cdot \vec{p_\perp}} \\
&\qquad \left(m_\perp K_1\left(nm_\perp \frac{\gamma_\perp(\vec{r}_\perp)}{T(\vec{r}_\perp)}\right) - \vec{p}_\perp \cdot \nabla_\perp \tau_f K_0\left(nm_\perp \frac{\gamma_\perp(\vec{r}_\perp)}{T(\vec{r}_\perp)}\right) \right)
\end{aligned}
\tag{1}
$$

Where the modified Bessel function enters the game. The azimuthal integral can thus be done analytically

$$
\begin{aligned}
\frac{dN_i}{dy\, m_\perp\, dm_\perp} &= \frac{g_i}{\pi^2} \sum_{n=1}^{\infty} (\pm)^n \int_0^{\infty} r_\perp dr_\perp\, \tau_f\, e^{n\mu_i/T} \\
&\qquad \left(m_\perp K_1\left(nm_\perp \frac{\gamma_\perp(\vec{r}_\perp)}{T(\vec{r}_\perp)}\right) I_0\left(n\frac{p_\perp v_\perp \gamma_\perp}{T}\right) \right. \\
&\qquad \left. -p_\perp \frac{\partial \tau_f}{\partial r_\perp} K_0\left(nm_\perp \frac{\gamma_\perp(\vec{r}_\perp)}{T(\vec{r}_\perp)}\right) I_1\left(n\frac{p_\perp v_\perp \gamma_\perp}{T}\right) \right)
\end{aligned}
\tag{2}
$$

And finally, defining $v_\perp = \tanh(\rho)$ and $\eta(\vec{r}_\perp) = \tau_f e^{n\mu_i/T}$, one obtains

$$\frac{dN_i}{dy\, m_\perp\, dm_\perp\, d\phi_p} = \frac{g_i}{\pi} \int_0^\infty r_\perp\, dr_\perp\, n_i(r_\perp) \left[m_\perp K_1 \left(\frac{m_\perp \cosh(\rho(r_\perp))}{T(r_\perp)} \right) \right.$$
$$I_0 \left(\frac{p_\perp \sinh(\rho(r_\perp))}{T(r_\perp)} \right) - p_\perp \frac{\partial \tau_f}{\partial r_\perp} K_0 \left(\frac{m_\perp \cosh(\rho(r_\perp))}{T(r_\perp)} \right) \quad (3)$$
$$\left. I_1 \left(\frac{p_\perp \sinh(\rho(r_\perp))}{T(r_\perp)} \right) \right]$$

.0.2 Appendice B

Under free-streaming the phase space distribution evolves as

$$f(\vec{r}, \vec{p}, t) = f(\vec{r} - \frac{\vec{p}}{E}(t - t_0), \vec{p}, t) \tag{4}$$

Using a Gaussian parametrization for the initial phase-space distribution of produced secondary particles

$$f(\vec{r}, \vec{p}, \tau) = e^{-\frac{x^2}{2R_x^2} - \frac{y^2}{2R_y^2} - \frac{p_x^2 + p_y^2}{2(\Delta\tau)^2}} \tag{5}$$

where Δt so writing the Eq 3.12 in integral form.

$$\epsilon_x = \frac{\int d^2 r r^2 \cos(2\psi_r \int d^3 p f(\vec{r}, \vec{p}, \tau))}{\int d^2 r r^2 \int d^3 p f(\vec{r}, \vec{p}, \tau)} \approx \frac{R_x^2 + R_y^2}{R_x^2 + R_y^2 + 2(c\Delta\tau)^2} \tag{6}$$

One get

$$\frac{\epsilon_x(t_0 + \Delta T)}{\epsilon_x(\tau_0)} = \left[1 + \frac{(c\Delta\tau)^2}{\langle \vec{r}^2 \rangle_{\tau_0}} \right]^{-1} \tag{7}$$

.0.3 Appendice C

For get the gran canonical partition function starting from Eq 3.19 visible below.

$$ln Z_i(T, V, \mu_i) = \frac{\Delta V g_i}{2\pi^2 \hbar^3} \int_0^\infty \theta_i p^2 dp \, \ln(1 + \theta_i e^{\beta(\mu_i - E)}) \tag{8}$$

replacing the logarithm with taylor expansion under the assumpion that $e^{\beta(\mu_i - E)} < 1 \rightarrow \mu_i < E$ and using $\lambda_i = e^{\beta \mu_i}$ it's possible to rewrite 3.1.

$$ln Z_i(T, V, \mu_i) = \frac{\Delta V g_i}{2\pi^2 \hbar^3} \sum_K \frac{(\theta \lambda_i)^k}{k} \int_0^\infty p^2 dp \, e^{-k\beta E} \tag{9}$$

integring by part

$$\ln Z_i(T, V, \mu_i) = \frac{\Delta V g_i}{2\pi^2 \hbar^3} \sum_K \frac{(\theta \lambda_i)^k}{k} \left[\frac{p^3 e^{-k\beta E}}{3} \Big|_0^\infty + \int_0^\infty dp \frac{p^3 \, k \, \beta e^{-k\beta E}}{3} \frac{dE}{dp} \right]$$
$$(10)$$

The first integrand vanish.

$$\frac{dE}{dp} = \frac{d}{dp}(\sqrt{p^2 + m_i^2}) = \frac{p}{\sqrt{p^2 + m_i^2}} = \frac{p}{E} \tag{11}$$

so

$$lnZ_i(T,V,\mu_i) = \frac{\Delta V g_i}{2\pi^2\hbar^3} \sum_K \frac{(\theta\lambda_i)^k}{k} \int_0^\infty dp \frac{p^3 \; k \; \beta e^{-k\beta E}}{3} \frac{E}{p} \tag{12}$$

introducing $x = k\beta E$, $w_i = k\beta m_i$ and $y_i = x/w_i$

$$lnZ_i(T,V,\mu_i) = \frac{\Delta V g_i}{2\pi^2\hbar^3} \sum_K \frac{(\theta\lambda_i)^k}{k} \int_0^\infty dE \frac{p^3 k\beta e^{-k\beta}}{3} \tag{13}$$

$$lnZ_i(T,V,\mu_i) = \frac{\Delta V g_i}{2\pi^2\hbar^3} \sum_K \frac{(\theta\lambda_i)^k}{k} \int_0^\infty dE \frac{(E^2 - m_i^2)^{3/2} k\beta e^{-k\beta}}{3} \tag{14}$$

$$lnZ_i(T,V,\mu_i) = \frac{\Delta V g_i m_i^2}{2\pi^2\hbar^3\beta} \sum_K \frac{(\theta\lambda_i)^k}{k^2} \int_0^\infty dE \frac{(x^2 - w_i^2)^{3/2}}{3w_i^2} e^{-x} \tag{15}$$

$$lnZ_i(T,V,\mu_i) = \frac{\Delta V g_i m_i^2}{6\pi^2\hbar^3\beta} \sum_K \frac{(\theta\lambda_i)^k w_i}{k^2} \int_0^\infty dE (\frac{x^2}{w_i^2} - 1)^{3/2} e^{-x} \tag{16}$$

$$lnZ_i(T,V,\mu_i) = \frac{\Delta V g_i m_i^2}{6\pi^2\hbar^3\beta} \sum_K \frac{(\theta\lambda_i)^k w_i}{k^2} \int_0^\infty dE w_i (y^2 - 1)^{3/2} e^{-w_i y} \tag{17}$$

introducing the modified Bessel function

$$k_2(q) = \frac{q^2}{3} \int_0^\infty dy (y^2 - 1)^{3/2} e^{-qy} \tag{18}$$

we finally obtain

$$lnZ_i(T,V,\mu_i) = \frac{\Delta V g_i}{2\pi^2\hbar^3\beta} \sum_K \frac{(\theta_i e^{\beta\mu_i})^k}{k^2} m_i^2 K_2(k\beta m_i) \tag{19}$$